An advanced inverse modeling framework for efficient and flexible adjoint-based history matching of geothermal fields

Tian, Xiaoming; Volkov, Oleg; Voskov, Denis

DOI
10.1016/j.geothermics.2023.102849

Publication date
2024

Document Version
Final published version

Published in
Geothermics

Citation (APA)
Tian, X., Volkov, O., & Voskov, D. (2024). An advanced inverse modeling framework for efficient and flexible adjoint-based history matching of geothermal fields. *Geothermics*, *116*, Article 102849. https://doi.org/10.1016/j.geothermics.2023.102849

Geothermics 116 (2024) 102849

Contents lists available at ScienceDirect

Geothermics

journal homepage: www.elsevier.com/locate/geothermics

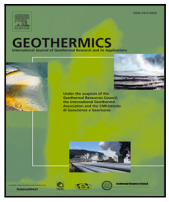

An advanced inverse modeling framework for efficient and flexible adjoint-based history matching of geothermal fields

Xiaoming Tian [a,c], Oleg Volkov [b], Denis Voskov [a,b,*]

[a] Department of Geoscience and Engineering, TU Delft, Delft, Netherlands
[b] Department of Energy Resources Engineering, Stanford University, CA, USA
[c] Guangzhou Institute of Energy Conversion, Chinese Academy of Sciences, Guangzhou, China

ARTICLE INFO

Keywords:
History matching
Principal Component Analysis
DARTS
Adjoint method
Geothermal energy

ABSTRACT

In this study, we present an efficient and flexible adjoint-based framework for history matching and forecasting geothermal energy extraction at a large scale. In this framework, we applied the Principal Component Analysis to reduce the parameter space for representing the complex geological model. The adjoint method is implemented for gradient calculation to speed up the history-matching iteration process. Operator-based linearization (OBL) used in this framework makes the calculation of the physical state and its derivatives very efficient and facilitates the matrix assembly in the adjoint method. This study primarily focuses on history matching based on combined observation of well production and in-situ electromagnetic measurements to predict the temperature front. However, different types of misfit terms can be added to the objective function based on practical considerations. For example, our history-matching case studies include model misfit terms applied for regularization purposes. The measurement data is extracted from the true model, and realistic measurement errors are considered. Also, in this work, we propose an optimal weighting strategy for the terms of the objective function to balance their sensitivity with respect to the model control variables. The high efficiency of the framework is demonstrated for the geothermal doublet model implemented at the heterogeneous reservoir with multiple realizations. The framework allows for generating posterior Randomized Maximum Likelihood (RML) estimates of the entire ensemble of the realizations with a reasonable computational cost. Results show that the framework can achieve reliable history-matching results based on the doublets production data and the reservoir electromagnetic measurement.

1. Introduction

A numerical simulation is an essential tool for developing geothermal resources. The most accurate resource estimations are achieved with high-fidelity simulations performed with physical models based on the first principles of mass and energy conservation (O'sullivan, 1985; Faust and Mercer, 1979; O'Sullivan et al., 2001; Wang et al., 2020). In order to calibrate such physical models, their response should be matched to geothermal field observations, which may include the observed well temperature, well flow rate, time-lapse data, etc. This calibration process is therefore called history matching and comprises the adjustment of uncertain geological model parameters, e.g., permeability, porosity, and thermal conductivity (Rath et al., 2006; Zhang et al., 2014; O'Sullivan and O'Sullivan, 2016; Zhang et al., 2019; Wu et al., 2021). Regarding geological uncertainty, the Bayesian approach is often adopted, taking into account all available prior knowledge, such as the hard data obtained from samples, geological formation scenarios, and assumptions on the statistical distribution. Essentially, Bayesian approach starts from the prior information on model parameters and uses observations (often with noise) to investigate the relation between the observation and the model parameters (Oliver et al., 2008; Hoteit et al., 2012). In this context, history matching has the goal to assimilate observed data and the prior parameters to generate a posterior estimate for the uncertain model. Typically, the observed data comprises the well water rates, bottom hole pressure (BHP), well temperature, and reservoir temperature distribution.

A limited research has been conducted on the history matching of geothermal reservoirs using electromagnetic observation data, though some investigation on history matching using the electromagnetic data in hydrocarbon reservoirs was performed, see for example (Zhang et al., 2019; Zhang and Hoteit, 2020). Electromagnetic (EM) data has recently been used in geothermal engineering for the interpretation of reservoir temperature distribution. EM data can be used to show the sensitivity to conductivity changes associated with fluid temperature

* Corresponding author at: Department of Geoscience and Engineering, TU Delft, Delft, Netherlands.
E-mail address: D.V.Voskov@tudelft.nl (D. Voskov).

https://doi.org/10.1016/j.geothermics.2023.102849
Received 14 March 2023; Received in revised form 9 September 2023; Accepted 17 October 2023
Available online 27 October 2023

fluctuations (Ucok et al., 1980; Sen and Goode, 1992). In our study, the reservoir temperature distribution interpreted from EM data is a crucial type of observation for the geothermal inverse modeling problem. This category of observation provides highly pertinent information for the gradient evaluation across the entire expanse of the reservoir, especially in the region where the reservoir temperature is changing because of the cold front propagation. It should be noted that EM data is not directly used in our study. Instead, the focus resides on employing the reservoir temperature interpreted from EM data as a pivotal observational input for our inverse modeling procedure.

Data assimilation can be performed in different ways, with methodologies having varying complexity and cost in terms of the number of numerical simulations required. Some methodologies, such as posterior sampling with Monte Carlo simulations, are straightforward to implement but are prohibitively expensive in conjunction with geothermal physical models (Rubinstein and Kroese, 2007; Nikolaidis et al., 2012; Adekitan, 2014). A more accessible way is to formulate and solve the history matching as an optimization problem where the observed historical data misfit is minimized at the same time as the statistical likelihood of the model parameters is maximized. This methodology has been applied in numerous works for the full statistics in the form of the Randomized Maximum Likelihood (RML) approach (see for example Oliver et al., 2008; Stordal and vdal, 2017) as well as for the reduced statistics in the form of Maximum A-Posteriori (MAP) estimate approach (see for example Vo and Durlofsky, 2014; Bukshtynov et al., 2015). In this paper, we adopt the RML approach for Electro-Magnetic (EM) monitoring and make it more efficient by coupling it with parameter space reduction as well as fast optimization and simulation techniques.

When considering the prior information in the history matching, the covariance matrix inversion is a serious issue. This issue is even more pronounced in the case of using a high-fidelity geological model. In this case, the dimension of the history matching problem needs to be reduced so that the problem can be solved in a lower dimensional space. This is reasonable because the history matching problem is usually over-parameterized for large models (Bukshtynov et al., 2015), as the amount of observation data is usually much smaller than the number of model parameters. Many methods for reducing the dimension have been widely investigated and applied in the field of geothermal, petroleum, and groundwater hydrology engineering.

Upscaling is one of the most often used methods to reduce the number of model parameters. In this method, a coarse grid model is applied to represent the high-resolution model by assigning the effective properties in each coarse cell (Durlofsky, 2005). Rühaak et al. (2015) investigated the upscaling of thermal conductivity of sedimentary formations for geothermal exploration. The results show that the harmonic averaging strategy is more accurate than other averaging methods. More upscaling approaches of hydraulic conductivity, permeability, and other petrophysical properties are analyzed in the reviews and studies of Sanchez-Vila et al. (2006), Neuman et al. (2013), and Wen and Gómez-Hernández (1996). However, consistent upscaling of geothermal models with convective and conductive flow still poses significant challenges (Perkins, 2019; Wang et al., 2023). For example, when employing local upscaling for non-reservoir lithologies, its applicability to basic flow simulations is evident, but its direct applicability to heat transfer encounters difficulties. This challenge arises due to the changes in heat outflow from upscaled volumes, surpassing fine grid simulation outcomes. Enhancements in accuracy are achieved through flow-based techniques, which involve re-evaluation of thermal transmissibility values. Nonetheless, accurately representing breakthrough times for large upscaled volumes remains an intricate task.

The upscaling can achieve high computational efficiency because of the reduced dimension that physically coarsens the model grid cells. Mathematically speaking, the degrees of freedom of the model can also be reduced by using fewer key components in the space, while these key components are mostly independent of each other and they represent and encapsulate the utmost essence of the original space. Principal Component Analysis (PCA) is a powerful tool to quantify the dependency among the components and boil down the key components under a specific criterion. PCA has been successfully applied in many history matching problems for multi-Gaussian fields (Gavalas et al., 1976; Oliver, 1996; Sarma et al., 2006). However, Sarma et al. (2007) pointed out that the direct use of PCA on non-Gaussian fields may lead to “Gaussian-looking” models after history matching. Therefore, they introduced kernel principal component analysis (KPCA) to solve this problem. Ma and Zabaras (2011) had later refined the KPCA approach. Although the KPCA approach focuses more on representing the multiple ‘‘feature’’ space in the reservoir, this method is essentially strongly nonlinear and brings challenging numerical issues. Vo and Durlofsky (2014) proposed an optimization-based PCA method for the low-dimensional parameterization of complex geological models. Bukshtynov et al. (2015) also introduced PCA parameterization in their gradient-based optimization framework for the closed-loop reservoir management problem. In their study, the adjoint method is applied and incorporated with the PCA parameterization to compute the new gradient in the reduced-dimension space.

Although lots of dimension reduction techniques can be applied to reservoir simulation problems, the low calculation efficiency is still a big issue that barricades the reservoir simulation on high-resolution models. To accelerate the physics calculation and improve overall computational efficiency, an Operator-Based Linearization (OBL) method was proposed and developed by Voskov (2017). This method was later incorporated into the newly proposed reservoir simulation framework Delft Advanced Research Terra Simulator (DARTS). Later, a higher simulation efficiency of DARTS has been achieved because of the adaptive parameterization of the physical parameter space and the implementation within GPU architecture. More details can be found in Khait and Voskov (2018b) and Khait et al. (2020).

We also developed the inverse modeling features in DARTS using the adjoint method. This method is applied to efficiently evaluate the gradient used in the optimization or history-matching problems. The idea of adjoint method is combining the original objective function with other constraints (e.g. the governing equations), while this procedure does not change the stationary point of the original objective function (Jansen, 2011). With the development of numerical reservoir simulations, this method was first applied to solve the history-matching problems in the petroleum recovery process (Mehos and Ramirez, 1989; Fathi and Ramirez, 1984; Ramirez et al., 1984), and it was further extended to the thermal recovery process (Wei et al., 1993). Tian et al. (2021) implemented the adjoint method for the generic multi-phase multi-component formulation and tested it on different ensembles of fluvial models. The result shows that, compared with the conventional numerical derivatives, several orders of magnitude in efficiency improvements are observed based on the adjoint method. The capabilities of inverse modeling in DARTS based on the adjoint gradients have been further extended in Tian and Voskov (2022) for the stochastic Discrete Well Affinity model.

In this study, the geothermal history matching and prediction using the reduced dimension technique are investigated. The PCA is applied to determine the dimension size of the reduced parameter space and find out the principal components to represent the reservoir model. We implement this framework in DARTS, which has the feature of simulating the geothermal developing process (Wang et al., 2020). We also extend the DARTS geothermal engine with the inversion feature of the adjoint method for gradient calculation in this study. To make the history-matching framework more flexible, various types of misfit terms can be added to the objective function based on practical considerations. We also propose an optimal weighting strategy for the terms of the objective function to balance their sensitivity with respect to the model parameters. The heterogeneous geological models of the fluvial field with 100 realizations (Jansen et al., 2014) are

utilized in this study to demonstrate the performance and high efficiency of this framework. This model is a synthetic reservoir featuring fluvial channels and it has been widely employed to illustrate aspects of computer-assisted flooding optimization and history matching. Its original "stochastic" form comprises 100 realizations of a channelized reservoir, using discrete permeability fields in a 60 × 60 × 7 grid (25,200 cells, 18,553 active). In this study, we make all 25,200 cells active. The high-permeability channels in a low-permeable background represent typical meandering river patterns as encountered in fluvial environments. The fields display a clear channel orientation with a typical channel distance and sinuosity. The permeability values have not been conditioned on the wells, while the porosity is assumed to be constant.

This paper proceeds as follows. In the next section, the mathematical descriptions of the geothermal forward simulation and the history-matching problem are presented. The adjoint method is also introduced. Next, the dimension reduction technique based on PCA is explained. In Section 4, an example of the modeling of electromagnetic response is utilized to test the proposed inverse modeling framework. The main results of the inverse modeling based on PCA parameterization under different training strategies are demonstrated in Section 5. The conclusion is provided in the last section.

2. Mathematical description

2.1. Forward modeling formulation

The geothermal model describes a non-isothermal process in which the heat is transported between fluids and surroundings in convective and conductive flows. In geothermal reservoir simulation, the governing equations describing this process consist of mass and energy conservation equations. The fully-coupled fully-implicit scheme is usually applied in the geothermal numerical simulation because this scheme is unconditionally stable. In DARTS, we adopted this scheme and used the finite volume method combined with two-point flux approximation to discretize the governing equations.

2.1.1. General formulation of geothermal system

Pressure and enthalpy are taken as the primary variables when solving the discretized equations. We assume that the influence of the chemical reactions on the mass and energy system is negligible. The governing questions of the geothermal system considering gravity effect are therefore given by:

$$\frac{\partial}{\partial t}\left(\phi\sum_{p=1}^{n_p}\rho_p s_p\right)-\mathrm{div}\sum_{p=1}^{n_p}\rho_p u_p+\sum_{p=1}^{n_p}\rho_p\tilde{q}_p=0, \tag{1}$$

$$\frac{\partial}{\partial t}\left(\phi\sum_{p=1}^{n_p}\rho_p s_p U_p+(1-\phi)U_r\right)-\mathrm{div}\sum_{p=1}^{n_p}h_p\rho_p u_p+\mathrm{div}(\kappa\nabla T)+\sum_{p=1}^{n_p}h_p\rho_p\tilde{q}_p=0, \tag{2}$$

where t is the time, ϕ is the porosity of porous media, n_p is the total number of the phases existing in the geothermal system, ρ_p is the density of phase p, s_p is the saturation of phase p, $\tilde{q}_p$ is the phase rate per unit volume, U_p is the phase internal energy, U_r is the internal energy of rock, h_p is the phase enthalpy, κ is the thermal conduction coefficient, T is the temperature.

The fluid Darcy velocity u_p considering gravity effect is:

$$u_p=\boldsymbol{K}\frac{k_{rp}}{\mu_p}\left(\nabla p_p-\gamma_p\nabla D\right), \tag{3}$$

where $\boldsymbol{K}$ is the permeability of porous media, k_{rp} is the phase relative permeability, μ_p is the phase viscosity, p_p is the pressure, γ_p is the specific weight, and D is the depth. The expression of porosity ϕ considering the rock compressibility is:

$$\phi=\phi_0\left(1+c_r\left(p-p_{ref}\right)\right), \tag{4}$$

where ϕ_0 is the initial porosity of the rock, c_r is the rock compressibility, and p_{ref} is the reference pressure.

In a geothermal system, there is only a single component (i.e., water), so the pressure and the enthalpy are taken as the primary variables (Wang et al., 2020). The pressure and enthalpy are then encapsulated and denoted as state variables $\boldsymbol{\omega}$. To solve the governing Eq. (1) and Eq. (2), Newton–Raphson method is applied:

$$\frac{\partial g\left(\boldsymbol{\omega}_k\right)}{\partial\boldsymbol{\omega}_k}\left(\boldsymbol{\omega}_{k+1}-\boldsymbol{\omega}_k\right)=-g\left(\boldsymbol{\omega}_k\right), \tag{5}$$

where g denotes the residual form of the governing Eq. (1) and Eq. (2), and the subscript k represents the kth nonlinear iteration.

The well treatment and the linearization of Eq. (1) and Eq. (2) using Operator-Based Linearization method can be found in Appendix B.

2.2. History matching problem

In this study, we formulate the history-matching problem as an optimization problem. An objective function is defined for this problem and it will be solved using the gradient-based method. The mathematical expression of the objective function usually contains two goals: (1) minimizing the data misfit between the observation and the model response and (2) minimizing the model misfit (or regularization) between the model parameters and the prior geological information. The data misfit term depends on the state variables $\boldsymbol{\omega}$ and the model control variables $\boldsymbol{u}$. Here the "control variable" corresponds to the "model parameter" that is often used in the Bayesian approach (or Bayes' theorem). The expression of the history matching problem therefore reads:

$$L(\boldsymbol{\omega},\boldsymbol{u})=\left(G(\boldsymbol{\omega},\boldsymbol{u})-\mathbf{d}_{\mathrm{obs}}\right)^T C_D^{-1}\left(G(\boldsymbol{\omega},\boldsymbol{u})-\mathbf{d}_{\mathrm{obs}}\right)+R, \tag{6}$$

where L is the objective function (i.e. loss function), G is the model response, $\mathbf{d}_{\mathrm{obs}}$ represents the observation data, C_D^{-1} is the inverse of the diagonal matrix characterizing measurement error, and R is the regularization term. Particularly in this work, the data misfit terms are formed by the weighted summation of the following expressions:

$$\begin{aligned}
f_1&=\sum_{j=1}^{\mathrm{n_w}}\sum_{p=1}^{\mathrm{n_p}}C_{j,p}^{rate}\left(q_{j,p}-q_{j,p}^*\right)^2\\
f_2&=\sum_{j=1}^{\mathrm{n_w}}C_j^{BHP}\left(p_j-p_j^*\right)^2\\
f_3&=\sum_{j=1}^{\mathrm{n_w}}C_j^{T_{well}}\left(T_j-T_j^*\right)^2\\
f_4&=\sum_{b=1}^{\mathrm{n_{block}}}C_b^{T_{res}}\left(T_b-T_b^*\right)^2,
\end{aligned} \tag{7}$$

where f_1, f_2, and f_3 are the misfit term of well flow rate, well BHP, and well block temperature, respectively. The term f_4 designates a proxy of the time-lapse electromagnetic (EM) data measurements represented via an effective reservoir block temperature. Here, $\mathrm{n_w}$ denotes the number of wells, $\mathrm{n_{block}}$ is the total number of reservoir blocks, $C_{j,p}^{rate}$, C_j^{BHP}, $C_j^{T_{well}}$, and $C_b^{T_{res}}$ are the corresponding diagonal elements of matrix C_D^{-1} in Eq. (6). The superscript $*$ denotes the observation data in the corresponding misfits.

Note that not all terms in Eq. (7) are necessarily included in Eq. (6). For example, when the wells are under rate control, we can remove the corresponding rate observation terms (i.e. f_1) while keeping the terms of BHP (i.e. f_2) in Eq. (6), and vice versa. The time-lapse data (i.e. f_4) can also be eliminated from Eq. (6) if the electromagnetic data measurements are not available. Furthermore, we proposed a weighting strategy for the terms in Eq. (7) to balance their sensitivity with respect to the model control variables by introducing the weighting factor D:

$$L(\boldsymbol{\omega},\boldsymbol{u})=\sum_{i=1}^{N}D_i f_i+R, \tag{8}$$

where N is the total number of the misfit term to be added to the objective function, and

$$D_i = \frac{1}{N f_{imax}}. \tag{9}$$

f_{imax} is the maximum value of f_i, which is usually obtained when the control variable is equal to the initial guess. This means that the misfit term of the objective function is always normalized to 1 before history matching.

The objective function given by equation Eq. (8) will be optimized through the utilization of the "L-BFGS-B" algorithm, which is available in the Python SciPy package. This algorithm requires the user to provide the objective function gradient, which will be employed by the optimizer to search for the minimum. Instead of calculating the gradient using the conventional numerical derivatives, which is very time-consuming, we utilize the adjoint method to calculate the gradient for the observation misfit term with significantly improved efficiency. The regularization term R only consists of the expression related to the model control variables. This indicates that the gradient of the regularization term can be easily calculated analytically. As for the gradient of the misfit terms, they are prepared using the adjoint method. More details about the implementation of the adjoint method on the misfit term can be found in the next section.

2.3. Adjoint gradients formulation

In the gradient descent method, calculating the gradient with respect to model control variables is not trivial work, especially when the degrees of freedom of the model control variables are very high. This is because the model responses (e.g., the well flow rates, well BHP, etc.) usually implicitly depend on the model control variables, so it is difficult to get the derivatives analytically, and sometimes it is even impossible. Alternatively, one may calculate the gradients using a numerical method. However, the numerical derivatives involve a large number of forward simulations, which is quite time-consuming. To obtain the gradient analytically and efficiently, the adjoint method is utilized in this study. More details about the adjoint method can be found in the review paper of Jansen (2011). Here we use the notation J to represent the misfit term of Eq. (6). Combined with the residual form of the governing equation, the augmented misfit term writes:

$$\mathcal{J}(\boldsymbol{\omega}, \boldsymbol{u}, \lambda) = \boldsymbol{J}(\boldsymbol{\omega}, \boldsymbol{u}) + \lambda^{\mathrm{T}} g(\boldsymbol{\omega}, \boldsymbol{u}), \tag{10}$$

where $\mathcal{J}$ denotes the augmented misfit term, $\boldsymbol{u}$ is the model control variables of the history matching problem, g is the residual form of the governing equation of the reservoir system, and λ^T is the transpose of Lagrange multipliers. To find the optimum of $\mathcal{J}$, we need to calculate its derivatives with respect to λ, $\boldsymbol{\omega}$ and $\boldsymbol{u}$, and make them equal to zero:

$$\mathcal{J}_{\lambda} = g(\boldsymbol{\omega}, \boldsymbol{u}) = 0, \tag{11}$$

$$\mathcal{J}_{\boldsymbol{\omega}} = \lambda^{\mathrm{T}} g_{\boldsymbol{\omega}}(\boldsymbol{\omega}, \boldsymbol{u}) + \boldsymbol{J}_{\boldsymbol{\omega}}(\boldsymbol{\omega}, \boldsymbol{u}) = 0, \tag{12}$$

$$\mathcal{J}_{\boldsymbol{u}} = \lambda^{\mathrm{T}} g_{\boldsymbol{u}}(\boldsymbol{\omega}, \boldsymbol{u}) + \boldsymbol{J}_{\boldsymbol{u}}(\boldsymbol{\omega}, \boldsymbol{u}) = 0, \tag{13}$$

where the subscript λ, $\boldsymbol{\omega}$ and $\boldsymbol{u}$ denotes the derivatives with respect to λ, $\boldsymbol{\omega}$ and $\boldsymbol{u}$, respectively. The Eq. (11) is actually the governing equation and is already satisfied in the forward simulation. As for Eqs. (12) and (13), they are known as adjoint equations and optimization equations, respectively. Note that $g_{\boldsymbol{\omega}}$, $g_{\boldsymbol{u}}$, $\boldsymbol{J}_{\boldsymbol{\omega}}$, and $\boldsymbol{J}_{\boldsymbol{u}}$ are easy to be collected thanks to the convenience of the OBL method. But before plugging in them to Eqs. (12) and (13), we need to introduce a Dirac function to make sure the consistency between the observation time points and the corresponding simulation time points. The misfit term $\boldsymbol{J}$, therefore, should be modified as:

$$\boldsymbol{J} = \sum_{k=1}^{K} (f_1^{(k)} + f_2^{(k)} + f_3^{(k)} + f_4^{(k)}) \delta_t(\mathrm{T_{obs}}), \tag{14}$$

where the superscript (k) denotes the kth simulation time step $\boldsymbol{\Delta t}_k$, K is the total number of the simulation time steps, $\delta_t(\mathrm{T_{obs}})$ is Dirac measure function and is given as:

$$\delta_t(\mathrm{T_{obs}}) = \begin{cases} 1 & \text{if } \mathrm{t} \in \mathrm{T_{obs}} \\ 0 & \text{if } \mathrm{t} \notin \mathrm{T_{obs}} \end{cases}, \tag{15}$$

where t is the time at the endpoint of time interval $\boldsymbol{\Delta t}_k$, $\mathrm{T_{obs}}$ is a set of the observation time points, which means it is a subset of the simulation time points. Now, with all necessary derivatives prepared, the adjoint gradient can be calculated by simply solving Eqs. (12) and (13). As it can be seen from Eq. (12), the Lagrange multiplier λ is solved backward in time. This backward-in-time procedure only consumes a similar computational time as a single forward simulation.

3. PCA-based parameterization

In the previous section, the adjoint method is introduced as an efficient approach for the evaluation of gradient. Nevertheless, the high dimensionality and uncertainty inherent in geological models still present notable obstacles to the optimizer's search for the global minimum. As previously noted, these obstacles can be addressed through the utilization of PCA approach, which enables the transformation of the original space into a reduced space. The uncertainty of the reservoir is usually quantified by an ensemble of geological realizations. Initially, the ensemble is generated based on all available prior geophysical information (e.g., hard data from the rock samples, seismic measurements, etc.). Then, the history matching process reduces further uncertainty. The uncertainty and the correlations among these realizations are described by a covariance matrix of the model control variables. Mathematically speaking, as long as the covariance (i.e., the off-diagonal elements in the covariance matrix) is non-zero, it means those model control variables depend on each other and, therefore, can be represented using fewer "independent" control variables in the parameter space. From the perspective of the history matching problem, the amount of observation data is much smaller than the number of unknown model parameters, so the history matching problem is over-parameterized for large models (Bukshtynov et al., 2015). This also indicates that the history matching problem is nonconvex, and the optimal solution is nonunique. The history matching, therefore, requires regularization term as shown in Eq. (6), and it writes:

$$R(\boldsymbol{u}) = \alpha_R (\boldsymbol{u} - \boldsymbol{u}_{ref})^T C_M^{-1} (\boldsymbol{u} - \boldsymbol{u}_{ref}), \tag{16}$$

where α_R is the scaling coefficient, C_M^{-1} is the inverse of the covariance matrix, and $\boldsymbol{u}_{ref}$ is the reference of the model control variables.

As mentioned above, the control variable space can be represented by using fewer "independent" variables in the new space. Here we utilize the Principal Component Analysis (PCA) to project the original ensemble of prior realizations into a new space characterized by a set of linearly uncorrelated variables. We denote the model control variables in the new space as $\boldsymbol{\xi}$.

The history matching based on Randomized Maximum Likelihood (RML) takes different samples of $\boldsymbol{u}$ as the $\boldsymbol{u}_{ref}$. Following the procedure of mapping the original model control variables $\boldsymbol{u}$ to $\boldsymbol{\xi}$ in Appendix C, the regularization terms Eq. (16) in the reduced-dimension $\boldsymbol{\xi}$-space should be written as:

$$\begin{aligned} \alpha_R (\boldsymbol{u} - \boldsymbol{u}_{ref})^T C_M^{-1} (\boldsymbol{u} - \boldsymbol{u}_{ref}) &= \alpha_R [\tilde{U} \tilde{\Sigma} (\boldsymbol{\xi} - \boldsymbol{\xi}_{ref})]^T (\tilde{U} \tilde{\Sigma}^{-2} \tilde{U}^T) [\tilde{U} \tilde{\Sigma} (\boldsymbol{\xi} - \boldsymbol{\xi}_{ref})] \\ &= \alpha_R [(\boldsymbol{\xi} - \boldsymbol{\xi}_{ref})^T \tilde{\Sigma} \tilde{U}^T] (\tilde{U} \tilde{\Sigma}^{-2} \tilde{U}^T) [\tilde{U} \tilde{\Sigma} (\boldsymbol{\xi} - \boldsymbol{\xi}_{ref})] \\ &= \alpha_R (\boldsymbol{\xi} - \boldsymbol{\xi}_{ref})^T (\boldsymbol{\xi} - \boldsymbol{\xi}_{ref}), \end{aligned} \tag{17}$$

where

$$\boldsymbol{\xi}_{ref} = \hat{\boldsymbol{\Phi}}^{-1} (\boldsymbol{u}_{ref} - \overline{\boldsymbol{u}}). \tag{18}$$

We will also check how the regularization affects the history-matching results if the model is constrained to the ensemble prior mean. In such

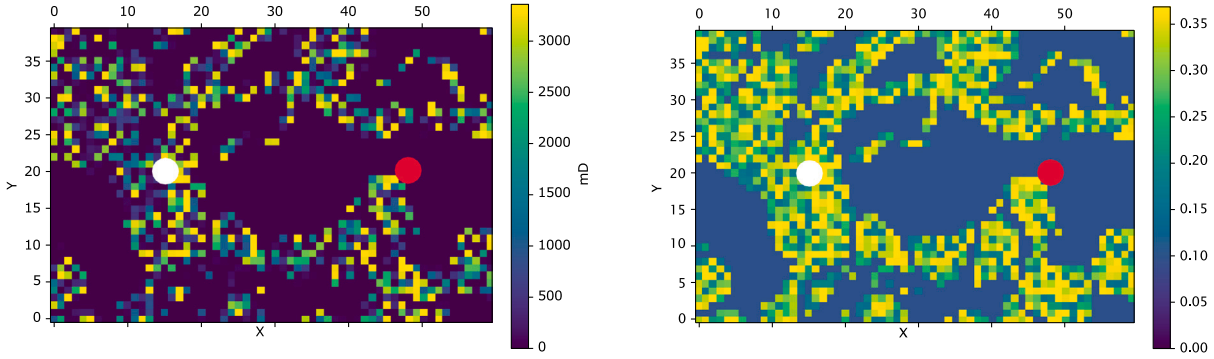

Fig. 1. The permeability map in the x direction (left) and the porosity map (right) of the 2D fluvial model. The white and red dots in the figures represent the well locations of the injector and the producer, respectively. (For interpretation of the references to color in this figure legend, the reader is referred to the web version of this article.)

Table 1
The parameters of 2D West Netherlands Basin model.

Model dimension	Production time	Initial temperature	Initial pressure	Rock conductivity
60 × 40 × 1 (30 m × 30 m × 2.5 m)	40 years	348.15 K	200 bars	200 kJ/m/day/K
Volumetric heat capacity	Well locations	Well depth	Well control of injector	Well control of producer
2200 kJ/m^3/K	15 × 20 × 1 (injector) 48 × 20 × 1 (producer)	1000 m	BHP control of 300 bars at 308.15 K	BHP control of 50 bars

case, the model reference $\boldsymbol{u}_{ref}$ is fixed as $\bar{\boldsymbol{u}}$. Therefore the regularization term is:

$$\alpha_R(\boldsymbol{u}-\boldsymbol{u}_{ref})^T C_M^{-1}(\boldsymbol{u}-\boldsymbol{u}_{ref}) = \alpha_R \boldsymbol{\xi}^T \boldsymbol{\xi}. \tag{19}$$

4. Modeling of electromagnetic response based on 2D model

In this section, we will present the application of the proposed framework on a 2D fluvial geothermal model. The electromagnetic monitoring data will be included in the objective function for history matching. Recently, there are some research about utilizing electromagnetic observations for the interpretation of field conductivity as it relates to temperature distribution. Notably, a three-dimensional simulator known as "emg3d" has been developed to facilitate diffusion EM modeling (Werthmüller et al., 2019). The behavior of the EM signal adheres to Maxwell's equations (Zhang et al., 2019). By assuming perfectly electrically conducting boundaries, employing a 1-meter-long electric dipole with a 1 A current source, and a relative permeability value of 1, the electric field can be determined through the governing equations. Subsequently, observations are acquired by sampling the electric field at designated receiver locations. It is important to highlight that this methodology utilizes the electric field's amplitude to avoid complex numbers in the recorded data. Extending the two-dimensional conductivity model along the z-axis yields three-dimensional outcomes. Through comparative analysis of field conductivity during different time-lapse intervals, deviations in field temperature can be deduced from alterations in field conductivity (Oudshoorn, 2023).

The proposed framework in this study does not necessarily require the time-lapsed field temperature values obtained from EM data. Instead, a singular field temperature observation at any given time step suffices (e.g., the temperature at the final time step) for conducting the inverse modeling. However, a greater number of field temperature observations across multiple time steps is advantageous, as inadequate temporal resolution may adversely impact the optimization solution of inverse modeling (Volkov and Voskov, 2015).

One of the synthetic geological layers from the West Netherlands Basin (Donselaar et al., 2015; Shetty et al., 2018) is taken as a 2D fluvial model. The permeability and porosity maps are shown in Fig. 1 . The parameters used in this model are shown in Table 1. The real time-lapse electromagnetic (EM) monitoring data is not available for this case study. Instead, we create an approximation of the temperature response interpreted from EM monitoring data. In our assumptions, the EM setup includes multiple surface sources and a single receiver in the production well that allowed us to fully reconstruct the temperature field. We will call this approximation of the temperature response as "EM data" in the following sections. The EM data will be used in the objective function f_4 of Eq. (7). For that, we collect the simulated temperature data and blur it by applying a spatial filtering kernel of the size that is consistent with the resolution scale of typical EM measurements. This synthetic EM data will be treated as the observations $\mathbf{d}_{\text{obs}}$. The steps are:

- Generate the true temperature data $\mathbf{d}_{\text{true}}$ based on the true model
- Compute the spatial filtering kernel size based on the r^2 to the EM receivers, where r is the distance between the given point and the EM receiver location. In this 2D model, we set the EM receiver at the location of the production well.
- Apply the spatial filtering strategy to the true temperature data based on the kernel size at different locations in the reservoir.

The flowchart depicting the aforementioned steps is illustrated in Fig. 2. The schematic of generating time-lapse EM data $\mathbf{d}_{\text{obs}}$ is shown in Fig. 3. The measurement error matrix C_D of EM data is computed based on the square of the difference between $\mathbf{d}_{\text{true}}$ and $\mathbf{d}_{\text{obs}}$.

Since the 2D model uses the BHP control as the well control, the misfit term of the objective function Eq. (6) consists of f_1, f_3, and f_4 from Eq. (7). The model is history matched based on the first 20 years of production and forecast for the next 20 years. The training and forecast curves are shown in Fig. 4. The results of the time-lapse temperature data are demonstrated in Fig. 5. As it can be seen from Fig. 4, the trained well rates and temperature match with the observation data very well, though the well temperature of the forecast period deviates a bit from the observation data. Fig. 5 also indicates a good history matching result of the time-lapse temperature data.

Note that the CPU time (Intel CPU i7-8556U) for a single forward simulation takes 2.1 s, while the gradient calculation using the adjoint method only takes 2.5 s for 4702 control variables in a single history-matching iteration. This means that the computational time used for

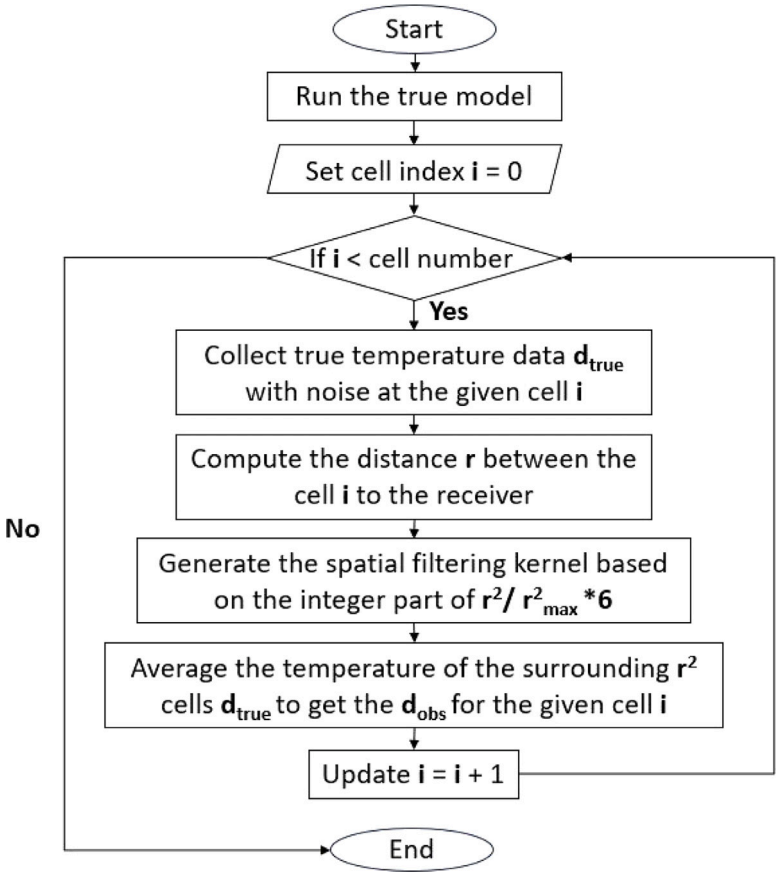

Fig. 2. The flowchart of generating synthetic time-lapse EM observation data.

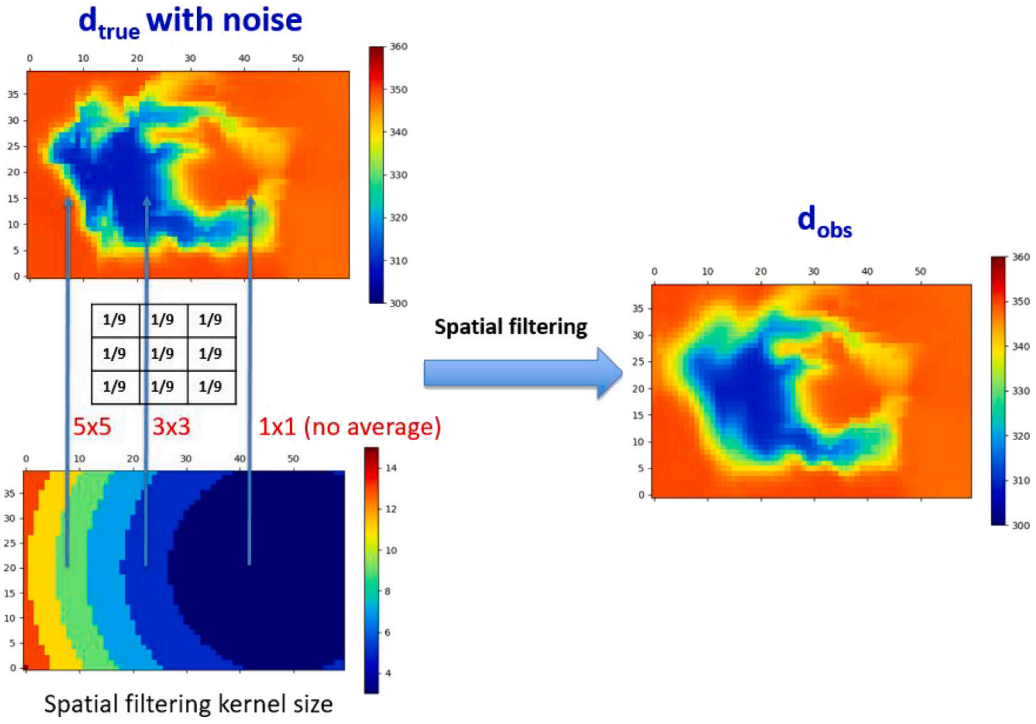

Fig. 3. The schematic of generating synthetic time-lapse EM data. Different levels of filtering kernels are applied at the given location of d_{true}(with noise) to generate synthetic EM observations d_{obs}. The accuracy of EM data diminishes as the distance between the given point and the location of the EM receiver increases.
Source: Adapted from Fig. 4 of Bukshtynov et al. (2015).

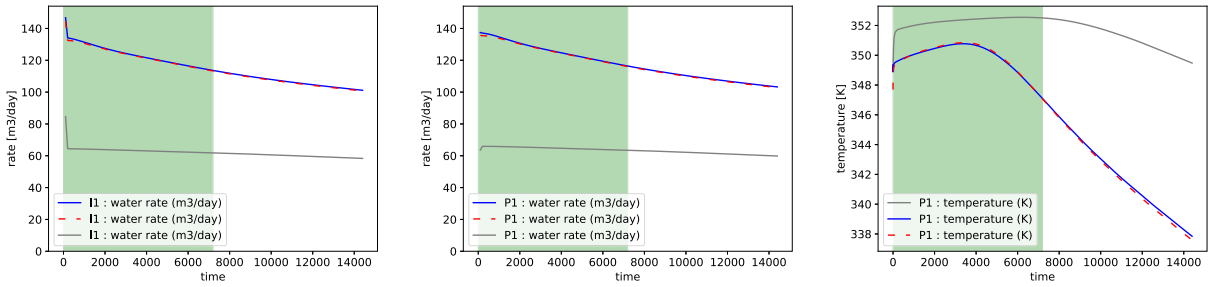

Fig. 4. The training and forecast results of the injection well rate (left), production well rate (middle), and production well temperature (right), respectively. The red dashed curves are the observation data. The gray and blue curves are the results before and after model training. The light green areas demonstrate the training periods while the rest areas are the forecast periods. (For interpretation of the references to color in this figure legend, the reader is referred to the web version of this article.)

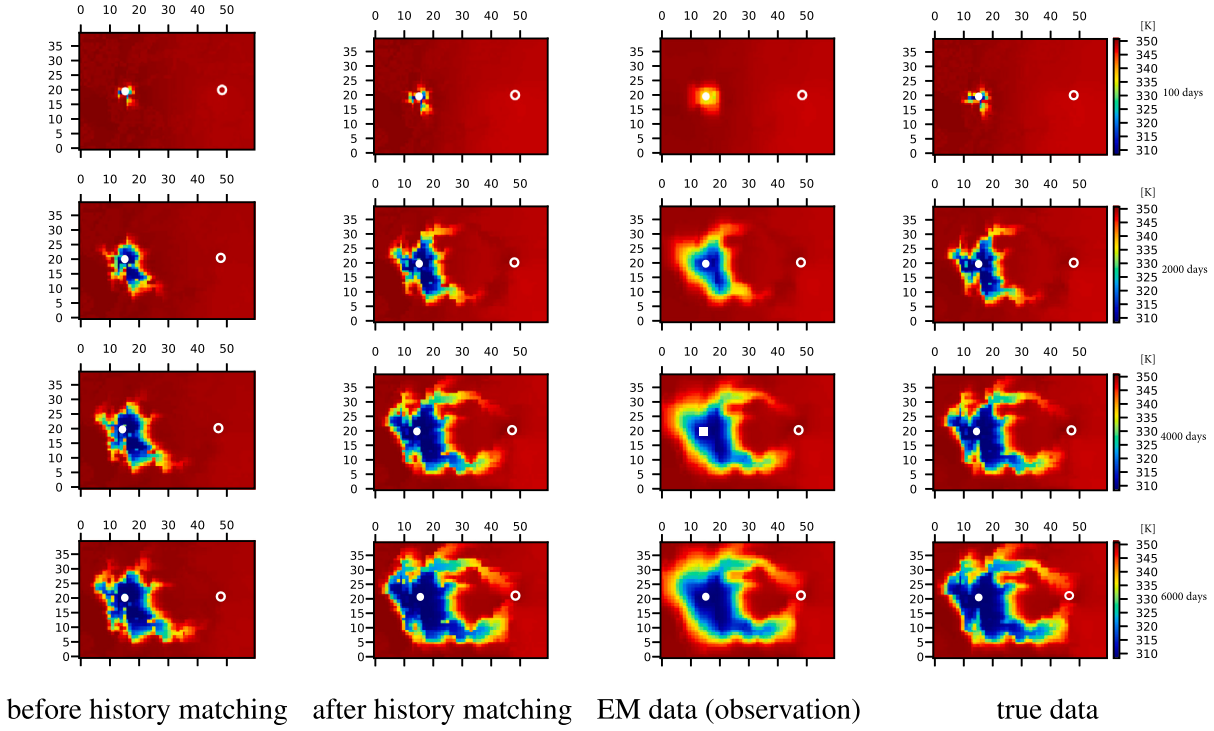

Fig. 5. The temperature distributions at different time steps. The white dot and circle show the well locations of the injector and producer, respectively. X and Y represent the cell index. From the top to the bottom rows, they represent the temperature distributions at the 100, 2000, 4000, and 6000 days respectively.

computing gradient is comparable to the CPU time of a single forward simulation, which is much less than the computational time of 4702 forward simulations used in the conventional numerical gradient calculation. This shows that the proposed framework based on the adjoint method has a significant improvement in the efficiency of the history matching problem. Next, we will present a more complex 3D example of the fluvial reservoir and introduce the dimension reduction technique based on the Principal Component Analysis method.

5. Simulation test using fluvial geothermal reservoir as prior model

In this section, a large ensemble of the fluvial models will be used in this study to demonstrate the history matching framework with PCA-based parameterization. Generally, when the degrees of freedom of the model are not so high, we can directly solve the history problem without using the dimension reduction technique. However, the high-resolution model usually brings a large number of degrees of freedom in the history matching problem. In this case, it may introduce redundant degrees of freedom to the problem. Moreover, if we try to conduct the history matching directly on the high-resolution model, it is often limited by the computer resources and capacities. With the concerns of the redundant degrees of freedom and the limitation of the computer capacity in the complex history matching problem, we introduce the dimension reduction technique into the proposed history matching framework.

We will use the fluvial models to demonstrate the process of dimension reduction in history matching. This model is an open-access geological reservoir ensemble (Jansen et al., 2014). This model consists of an ensemble of 100 permeability realizations of a three-dimensional channelized reservoir. The term "realization #n" hereafter denotes the nth realization of the original set. The realization #1 will be considered a "true" model to generate the observation data. The rest of the 99 realizations will be used as priors to train the model. The permeability data are imported from the ensemble realizations. The permeability in the x and y directions are identical, while the permeability in the z direction is 0.1 times the horizontal permeability. The uniform properties of porosity, pressure, initial reservoir temperature, the volumetric heat capacity of rock, and the thermal conductivity of rock are shown in Table 2. A doublet (one injector and one producer) is set in the reservoir with all seven layers perforated, see Fig. 6. The true model "realization #1" will run for 40 years to generate the observation data. The first

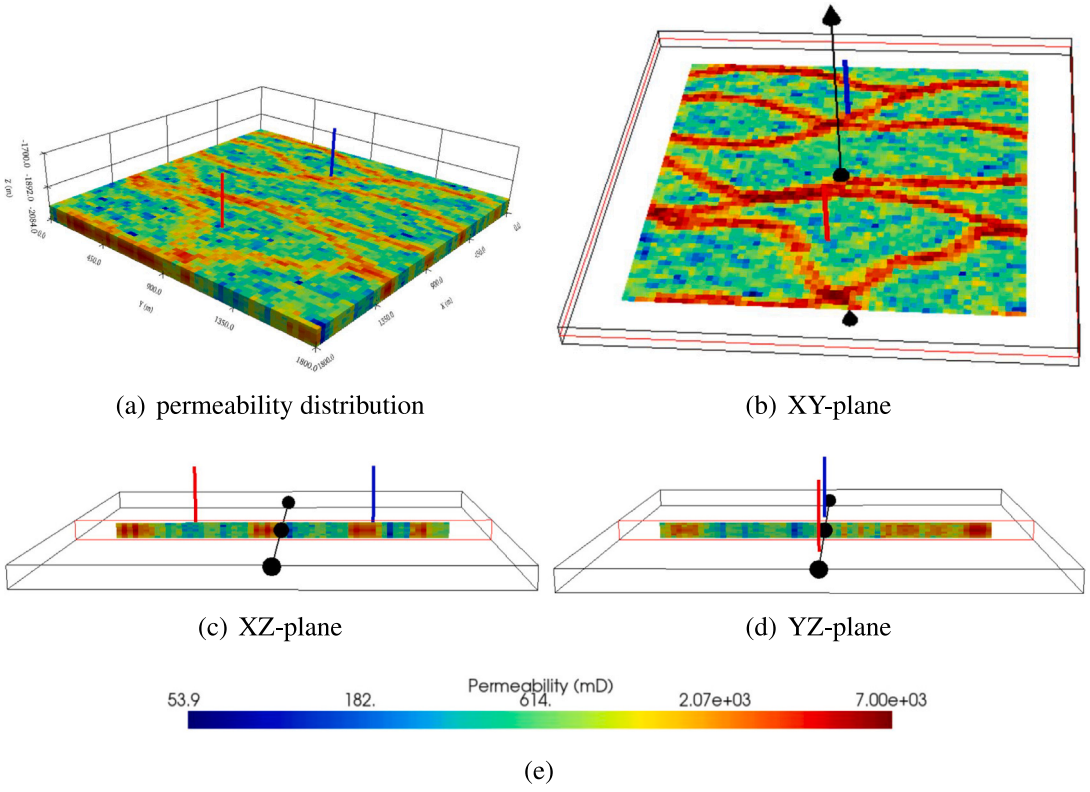

Fig. 6. The permeability distribution of realization #1. The blue and red bars represent the location of the injector and producer, respectively. (For interpretation of the references to color in this figure legend, the reader is referred to the web version of this article.)

Table 2
The parameters of 3D fluvial model.

Model dimension	Production time	Initial temperature	Initial pressure	Rock conductivity
60 × 60 × 7 (30 m × 30 m × 12 m)	40 years	348.15 K	200 bars	181.44 kJ/m/day/K
Volumetric heat capacity	Well locations	Well depth	Well control of injector	Well control of producer
2200 kJ/m^3/K	14 × 30 × 1 to 7 (injector) 46 × 30 × 1 to 7 (producer)	2000 m	Rate control of 5000 m^3/day at 308.15 K	Rate control of 5000 m^3/day

30 years are taken as the training period, and the rest 10 years are the forecast period to test the performance of the proposed method.

Following the dimension reduction process described in Section 3 and Eq. (C.13), the dimension of the control variable space of transmissibility is reduced to 82. The total number of the dimension is therefore 82 plus 14 (well indexes). This is much less than the original dimension of the transmissibility (i.e., 71160 block interfaces) and well indexes (i.e., 14 perforation positions) control variable space. The time-lapse electromagnetic data are also included in the objective function to train the model. The history matching process of most of the priors can be finished within 8 h. The total training time of 99 realizations is 10 h on DelftBlue cluster (Delft High Performance Computing Centre (DHPC), 2022) with multiple nodes and cores of 2x Intel XEON E5-6248R 24C 3.0 GHz processors.

5.1. The training based on maximum likelihood estimation

In the Maximum Likelihood Estimation (MLE) method, we will show the history matching results without the consideration of regularization. This means, compared with Bayes' theorem, only the likelihood will be maximized, while the prior information is not considered.

The history matching results of well temperature are shown in Fig. 7. Except for a few realizations that are relatively far from the observation data (red curve), most of the trained realizations have good history matching results (the green area in the figure) to the observation data. Although the forecasting results (the white area in the figure) demonstrate a wider range of well temperature, this is expected and acceptable for the forecasting period. Here we introduce Root Mean Square Error (RMSE) to quantify the error of the results. The expression of RMSE is given as:

$$RMSE = \sqrt{\frac{\sum_{i=1}^{N} \left(G - \mathbf{d}_{\text{true}}\right)^2}{N}} \tag{20}$$

where G is the model response and $\mathbf{d}_{\text{true}}$ is the true data. For each realization, the RMSE can be calculated based on Eq. (20). The ensemble average RMSE for MLE is 0.253.

The history matching results of reservoir temperature data are shown in Fig. 8. This figure shows the temperature results of the 4th layer of realization #66. It can be clearly seen that the temperature results after the history matching have a good match with the EM observation data, even though the original temperature distribution is very different from the observed EM data. This indicates that the optimizer might have largely changed the original permeability distribution of realization #66 to try to match the EM observation data. Therefore,

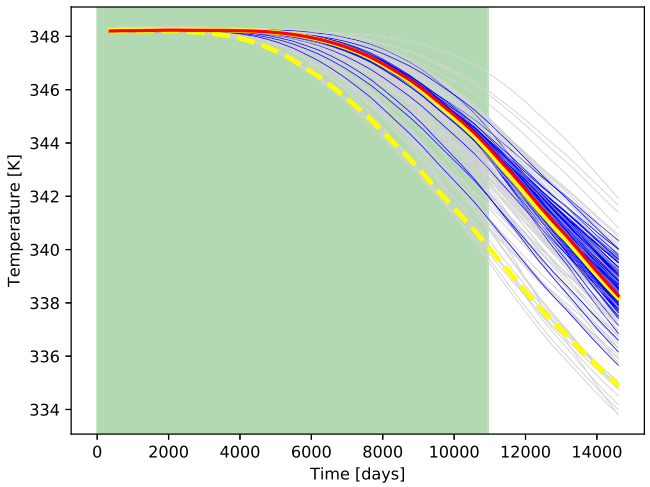

Fig. 7. The history matching results of the well temperature for the entire ensemble of the fluvial model based on MLE. The red curve is the observation data of well temperature. The gray and blue curves are the results before and after history matching, respectively. The yellow dashed and solid lines represent the results of realization #66 before and after history matching. The green area shows the training period, while the white area is the forecasting period. (For interpretation of the references to color in this figure legend, the reader is referred to the web version of this article.)

we plot the permeability distribution of this realization and the "true" permeability distribution in Fig. 9.

Fig. 9 shows the permeability of realization #66 before (figure a) and after (figure b) history matching. The true permeability (figure c) and the difference (figure d) between the permeability before and after history matching are also presented. As it can be seen from the figure (d) in Fig. 9, the optimizer tries to block the original fluvial channel (blue channelized area), while reconstruct the channel of the "true" model (red channelized area). This is because, with the information given by observed EM data, the adjoint gradient is able to capture the characteristics of the "true" permeability field, and therefore reconstruct the temperature map that is similar to the observed EM data.

In the next section, we will repeat this history matching procedure, while considering the prior information of the realization permeability based on Bayes' theorem. The reduced-dimension technique based on PCA is also introduced.

5.2. The training based on randomized maximum likelihood

In the Randomized Maximum Likelihood method (RML), the prior information is considered and the regularization term chooses each realization from the ensemble as the reference model. Therefore, the regularization term in the reduced-dimension ξ-space is written as Eq. (17). A comparison of RML in the original space and reduced-dimension ξ-space can be found in Appendix A. The history matching results of well temperature is shown in Fig. 10. The ensemble average RMSE is 0.314. Compared with the history matching based on MLE shown in the previous section, the well temperature curves of the entire ensemble have a wider distribution range around the observation data curve (red curve) and a larger ensemble average RMSE. This is because the regularization term forces the optimizer to search the optimum around the prior, instead of searching in an area that is far away from the prior in the parameter space. From Bayes' theorem perspective, this history-matching procedure considered both the prior knowledge and the likelihood maximization.

To compare with the history-matching results of the previous section, we also take the 4th layer of realization #66 as an example to show the history-matching results of reservoir temperature data and permeability map based on RML. They are demonstrated in Figs. 11 and 12. It can be seen from Fig. 11 that the history-matching result of reservoir temperature based on RML has less similarity to the results of the previous section (i.e. MLE method). This is because, with regularization, the optimizer tends to preserve the prior information instead of severely reforming the prior to maximize the likelihood. This is also reflected in the permeability difference map (i.e. figure (d)) in Fig. 12. The permeability distribution is not significantly changed compared with the permeability difference map in Fig. 9, though there are still some slight permeability modifications along the prior fluvial channel (i.e. blueish color in the permeability difference map).

5.3. The training constrained to ensemble prior mean

We also conducted the history matching to explore the impact of regularization on history matching outcomes when the model is constrained to the ensemble prior mean. In this case, the reference model used in regularization is fixed with the average of the whole realization ensemble. The regularization term in the reduced-dimension ξ-space is therefore shown as in Eq. (19).

The history matching results of the well temperature are shown in Fig. 13. The ensemble average RMSE is 0.312. Similarly, we take the 4th layer of realization #66 as an example to show the results of reservoir temperature data and permeability map in Figs. 14 and 15.

We do not observe the evident difference between this method and RML. This might be because, with the regularization term, the optimizer is prone to search for the optimum around the initial guess therefore trapped in the local minimum that is close to the initial guess. This phenomenon is as expected, considering the high heterogeneity and the fluvial channels existing in the fluvial model.

5.4. Comparisons of history matching methods

When conducting the history matching using these three types of methods, we distribute the history matching tasks to different nodes and cores on DelftBlue cluster (Delft High Performance Computing Centre (DHPC), 2022), specifically, one core per simulation. This cluster is equipped with 2x Intel XEON E5-6248R 24C 3.0 GHz processors.

The comparison between these three types of history matching results is demonstrated in Fig. 16. The RMSE, CPU time, and degrees of freedom (DoF) of each method are demonstrated in Table 3. The reported CPU time is the mean duration of history matching computations across the entire ensemble of realizations. It is worth noticing that even though the RML with full space uses the least CPU time of 2.94 h, it needs an extra 16.33 h to inverse the full covariance matrix and it yields the highest RMSE of 0.564. In contrast, the history matching based on MLE has the lowest RMSE of 0.253, though it takes a somewhat extended duration of time for the optimal solution search.

6. Conclusions

An efficient and flexible adjoint-based history-matching framework for the geothermal reservoir is proposed and developed in this study. To ensure scalability, high-performance optimization and space reduction techniques are introduced and implemented in this framework.

The adjoint method is successfully implemented into the DARTS simulator for the geothermal engine. With the application of the adjoint method, the calculation efficiency and accuracy of the gradient used in the history matching iterations are largely improved. This advancement empowers the framework to effectively conduct history-matching iterations involving a vast number of control variables, which is a critical capability in geothermal reservoir management. In this study, the history matching of the fluvial model with the impressive control variable number of 71,160 can be finished within a relatively short timeframe of 10 h on an Intel XEON E5-6248R processor. In

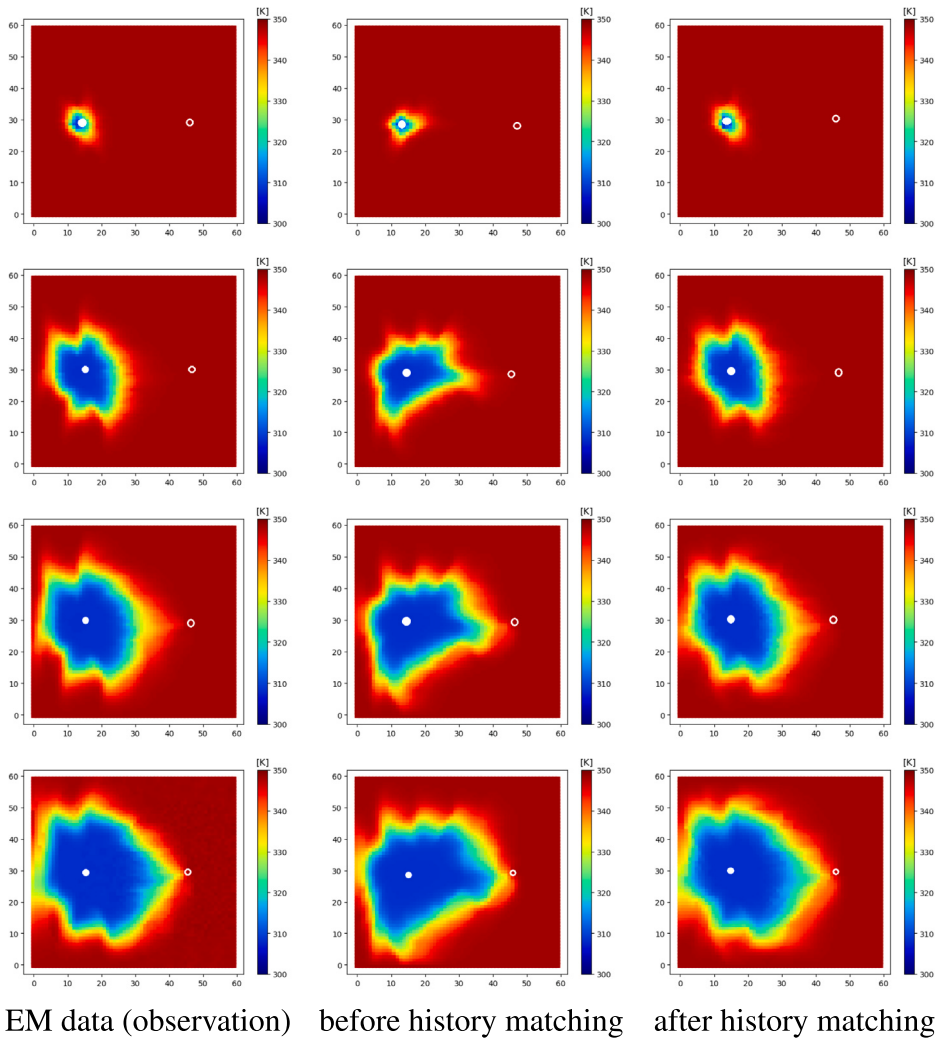

Fig. 8. The history matching results of the reservoir temperature of the 4th layer of the fluvial model. The left column shows the temperature observation data derived from EM data of the "true" model. The middle and right columns are the results of realization #66 based on MLE. From the top to the bottom rows, they represent the temperature distributions at 1, 10, 20, and 30 years respectively. The white dots and circles represent the injector and producer, respectively.

Table 3
The RMSE, mean CPU time, and degrees of freedom of the model parameters for each method.

	MLE	RML(full space)	RML	HM constrained to ensemble prior mean
RMSE	0.253	0.564	0.314	0.312
Mean CPU time [h]	9.18	2.94+(16.33)	6.31	6.80
DoF of space	71174	71174	96	96

contrast, the history matching with a control variable of equivalent magnitude through conventional numerical gradient calculated via the Finite Difference Method is basically unfeasible.

To represent the complexity of the model while keeping the uncertainty of the model ensemble, the Principal Component Analysis is utilized to transform the model from the original space to the reduced-dimension ξ space, and vice versa. This procedure involves the transformation of the control variables, gradients, and regularization terms.

The time-lapse temperature distribution data derived from electromagnetic data measurements have been also considered in the proposed history matching framework. Here, we assumed that by using multiple sources and single receiver in the production well, we can fully reconstruct the temperature field. Combined with the conventional observations of well rates and BHP, the trained model is able to predict the temperature front. However, it is not necessary to include all types of observations in this history-matching framework. The framework

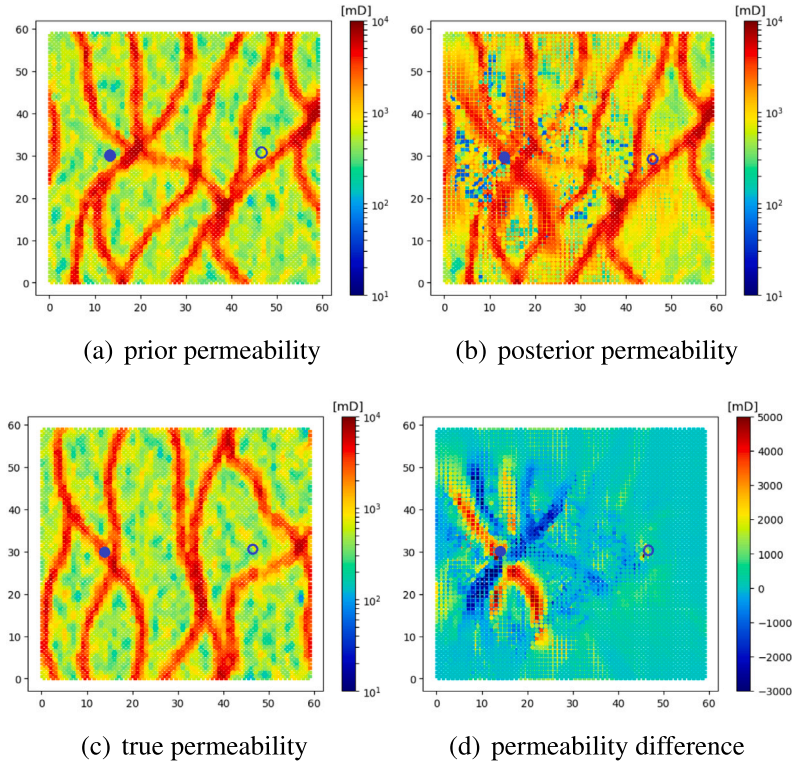

Fig. 9. The permeability distribution of the 4th layer of fluvial model. Figure (a) demonstrates the prior permeability of realization #66 before history matching; (b) is the posterior permeability after history matching; (c) shows the "true" permeability; and (d) demonstrates the permeability difference between posterior and prior based on MLE. The blue dots and circles represent the injector and producer, respectively. (For interpretation of the references to color in this figure legend, the reader is referred to the web version of this article.)

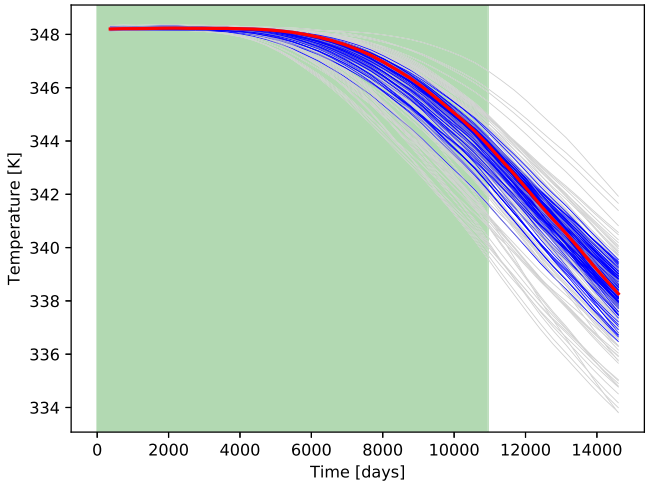

Fig. 10. The history matching results of the well temperature based on RML under the reduced-dimension ξ-space. The red curve is the observation data of well temperature. The gray and blue curves are the results before and after history matching, respectively. The green area shows the training period, while the white area is the forecasting period. (For interpretation of the references to color in this figure legend, the reader is referred to the web version of this article.)

provides the flexibility of adding or removing different types of observations in the objective function based on the availability and necessity of the observation data.

The comparison of the history matching based on MLE, RML, and constrained to ensemble prior mean, are presented in this study to illustrate the performance of the proposed framework. The results show that the adjoint gradients can capture the characteristics of the "true" permeability field and re-construct the temperature map that is observed from the EM data. This phenomenon is especially pronounced in the history matching based on MLE. In the history matching based on RML and the case constrained to the ensemble prior mean, the history matching considers both the likelihood maximization and the prior knowledge information. Therefore, the model response has relatively less similarity to the observation, while the prior permeability information is preserved.

The significance of this efficient and flexible history-matching framework lies in its capacity to streamline the calibration process of geothermal reservoir models, thus enhancing predictive accuracy and facilitating optimal decision-making in geothermal reservoir management. With the ability to handle a large number of control variables efficiently, geothermal practitioners can gain deeper insights into reservoir behavior, which in turn aids in the sustainable and effective utilization of geothermal resources.

In this study, we use a 3D model with less heterogeneity along the vertical direction, and the reservoir temperature and pressure are uniformly initialized. In future work, we may consider more heterogeneous and high-enthalpy models. The adjoint method for Multi-Point Flux Approximation simulator may also be developed.

CRediT authorship contribution statement

Xiaoming Tian: Writing – original draft, Software, Data curation, Reviewing & editing. **Oleg Volkov:** Conceptualization, Methodology, Reviewing. **Denis Voskov:** Supervision, Conceptualization, Methodology, Reviewing & editing.

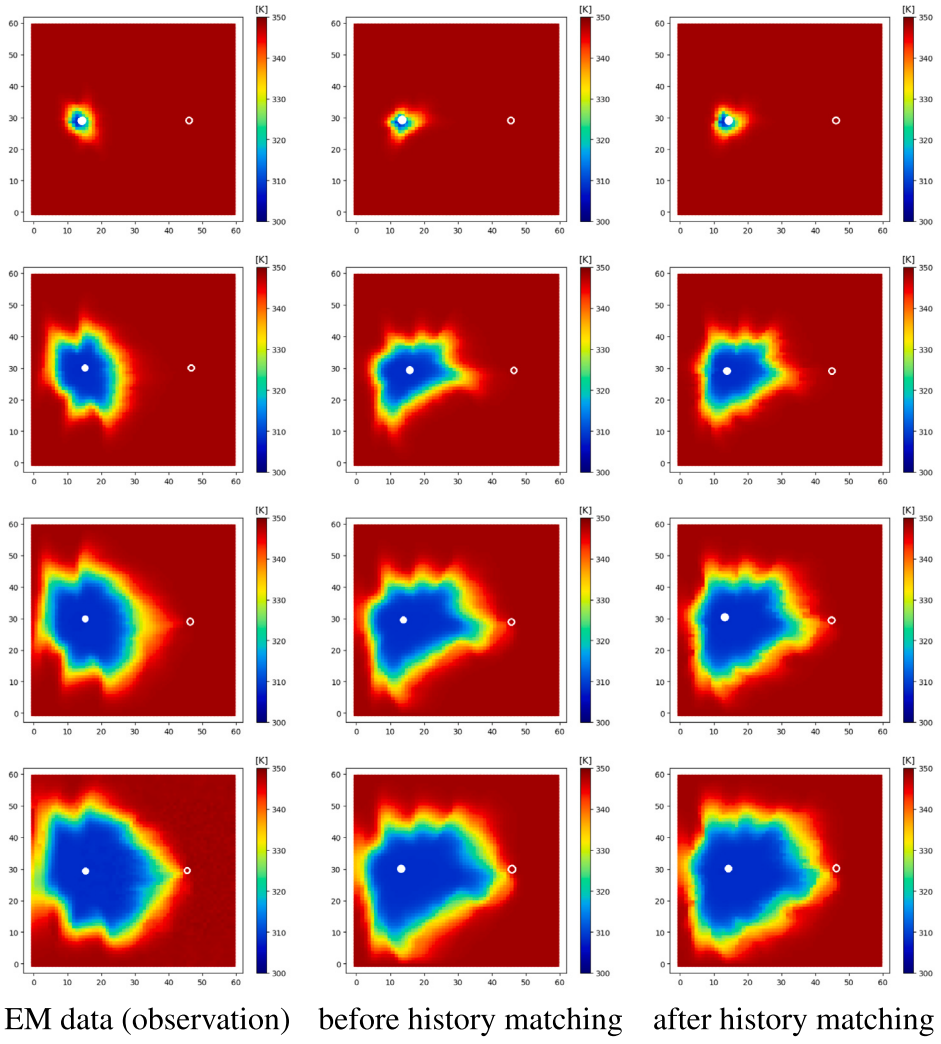

Fig. 11. The history matching results of the reservoir temperature of the 4th layer of fluvial model. The left column shows the temperature observation data derived from EM data of the "true" model. The middle and right columns are the results of realization #66 based on RML. From the top to the bottom rows, they represent the temperature distributions at 1, 10, 20, and 30 years respectively. The white dots and circles represent the injector and producer, respectively.

Declaration of competing interest

The authors declare the following financial interests/personal relationships which may be considered as potential competing interests: Xiaoming Tian reports financial support was provided by China Scholarship Council.

Data availability

Data will be made available on request.

Acknowledgments

We would like to thank Evert Slob for his valuable suggestions about the part of the electromagnetic measurement and China Scholarship Council (CSC) for the financial support of X. Tian. We also gratefully acknowledge support from the industrial affiliates of the Stanford Smart Fields Consortium.

Appendix A

A comparison of RML in the original full space and reduced-dimension ξ-space was conducted to check the feasibility and the accuracy of the reduced-dimension technique based on PCA. As shown in Eq. (16), the RML in the original full space requires the inversion of covariance matrix C_M of control variables. In the fluvial reservoir model, the control variables have a dimension of 71,160 (i.e. the transmissibility of the interfaces of reservoir blocks). This indicates large amounts of computational cost and memory consumption for the matrix inversion. To inverse a non-positive definite covariance matrix, the pseudo-inverse function from the Python Numpy linear algebra package is chosen to inverse C_M. This inversion procedure needs around 500 GB of memory and takes more than one day to finish the computation. Finally, the output inversed covariance matrix C_M^{-1} has a size of 39.6 GB and can be stored for further use in each realization in the ensemble.

The history matching results of well temperature are shown in Fig. A.17. It is evident to see that the history matching has a more divergent result in the original full space, compared with the result in the reduced-dimension ξ-space. Their ensemble average RMSEs are

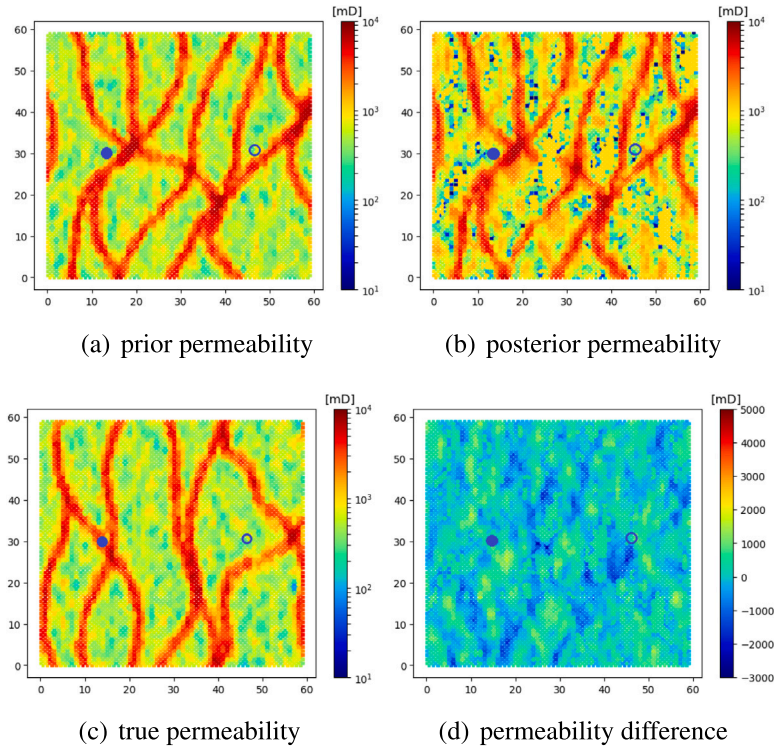

Fig. 12. The permeability distribution of the 4th layer of fluvial model. Figure (a) demonstrates the prior permeability of realization #66 before history matching; (b) is the posterior permeability after history matching; (c) shows the "true" permeability; and (d) demonstrates the permeability difference between posterior and prior based on RML. The blue dots and circles represent the injector and producer, respectively. (For interpretation of the references to color in this figure legend, the reader is referred to the web version of this article.)

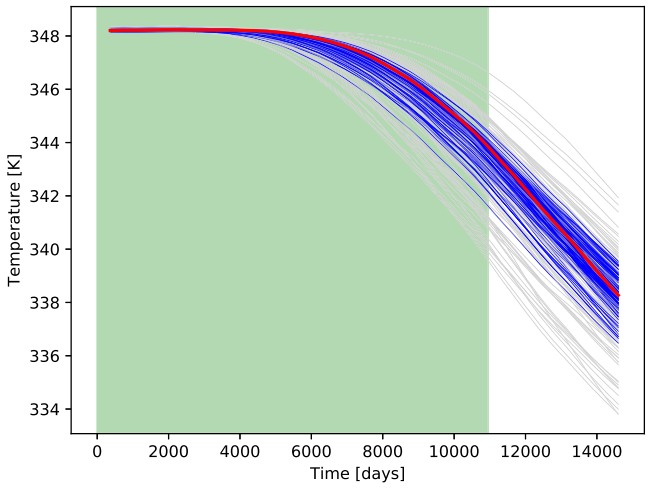

Fig. 13. The results of the history matching constrained to the ensemble prior mean under the reduced-dimension ξ-space. The red curve is the observation data of well temperature. The gray and blue curves are the results before and after history matching, respectively. The green area shows the training period, while the white area is the forecasting period. (For interpretation of the references to color in this figure legend, the reader is referred to the web version of this article.)

0.564 and 0.314, respectively. It indicates that the reduced-dimension technique based on PCA is capable of generating more accurate history-matching results. Moreover, this technique requires much less machine memory and computational time to evaluate the regularization term.

Appendix B

Operator-Based Linearization

Based on the Operator-Based Linearization (OBL) approach for geothermal system (Wang et al., 2020), the discretized mass conservation equation in operator form for a given gridblock i is:

$$\phi_0 V\left(\alpha(\boldsymbol{\omega})-\alpha\left(\boldsymbol{\omega}_n\right)\right)+\sum_l \Delta t \Gamma^l \sum_{p=1}^{n_p} \boldsymbol{\Phi}_{p,ij}\beta_p(\boldsymbol{\omega})=0. \tag{B.1}$$

Here we omit most of the gridblock index i in this equation, $\boldsymbol{\omega}_n$ represents the state variable a the previous time step, l is the interface between two neighboring gridblocks, Γ^l is the transmissibility at the interface l, and the state-dependent operators α and β are written as:

$$\begin{aligned}\alpha(\boldsymbol{\omega})&=\left(1+c_r\left(p-p_{ref}\right)\right)\sum_{p=1}^{n_p}\rho_p s_p,\\ \beta_p(\boldsymbol{\omega})&=\rho_p\frac{k_{rp}}{\mu_p},\end{aligned} \tag{B.2}$$

The phase potential difference $\boldsymbol{\Phi}_{p,ij}$ in Eq. (B.1) is defined based on phase-potential-upwinding (PPU) strategy (Khait and Voskov, 2018a):

$$\boldsymbol{\Phi}_{p,ij}=p_j-p_i-\frac{\delta_p\left(\boldsymbol{\omega}_i\right)+\delta_p\left(\boldsymbol{\omega}_j\right)}{2}\left(D_j-D_i\right), \tag{B.3}$$

where the subscript i and j are the index of gridblock i and j respectively, δ_p is the density operator for phase p.

The discretized energy equation in operator form is written as:

$$\begin{aligned}&\phi_0 V\left[\alpha_{ef}(\boldsymbol{\omega})-\alpha_{ef}\left(\boldsymbol{\omega}_n\right)\right]+\left(1-\phi_0\right)VU_r\left[\alpha_{er}(\boldsymbol{\omega})-\alpha_{er}\left(\boldsymbol{\omega}_{k-1}\right)\right]\\ &\quad+\sum_l \Delta t\Gamma^l\sum_{p=1}^{n_p}\boldsymbol{\Phi}_{p,ij}\beta_{ep}(\boldsymbol{\omega})\\ &\quad+\sum_l \Delta t\Gamma_e^l\left(T^i-T^j\right)\left[\phi_0\gamma_{ef}(\boldsymbol{\omega})+\left(1-\phi_0\right)\kappa_r\gamma_{er}(\boldsymbol{\omega})\right]=0,\end{aligned} \tag{B.4}$$

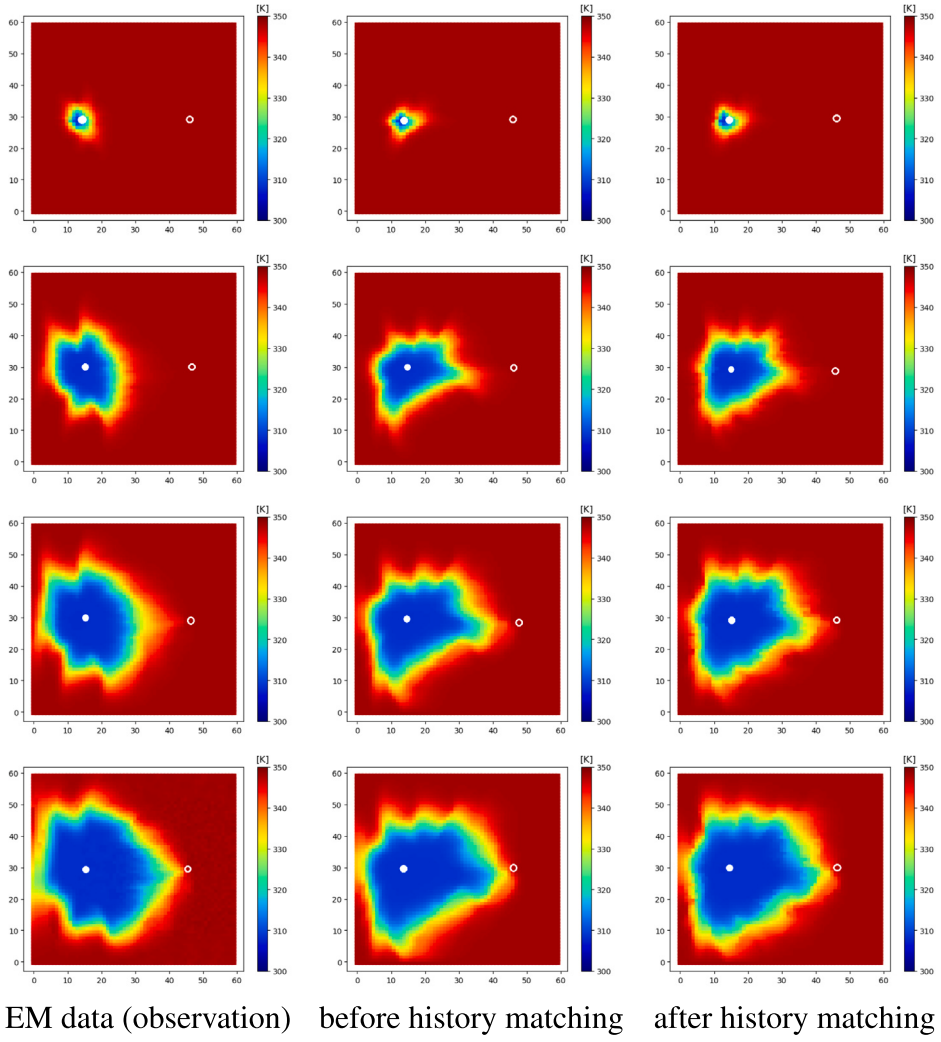

Fig. 14. The history matching results of the reservoir temperature of the 4th layer of fluvial model. The left column shows the temperature observation data derived from EM data of the "true" model. The middle and right columns are the results of history matching constrained to the ensemble's prior mean. From the top to the bottom rows, they represent the temperature distributions at 1, 10, 20, and 30 years respectively. The white dots and circles represent the injector and producer, respectively.

where Γ_e^l is the coefficient related to thermal transmissibility, and the operators are defined as:

$$\begin{aligned}
\alpha_{ef}(\boldsymbol{\omega}) &= \left(1 + c_r\left(p - p_{ref}\right)\right)\sum_{p=1}^{n_p}\rho_p s_p U_p,\\
\alpha_{er}(\boldsymbol{\omega}) &= \frac{1}{1 + c_r\left(p - p_{ref}\right)},\\
\beta_{ep}(\boldsymbol{\omega}) &= h_p\rho_p\frac{k_{rp}}{\mu_p},\\
\gamma_{ef}(\boldsymbol{\omega}) &= \left(1 + c_r\left(p - p_{ref}\right)\right)\sum_{p=1}^{n_p}s_p\kappa_p,\\
\gamma_{er}(\boldsymbol{\omega}) &= \alpha_{er}(\boldsymbol{\omega}).
\end{aligned} \tag{B.5}$$

Note that the operators in Eq. (B.2) and Eq. (B.5) are only dependent on physical state $\boldsymbol{\omega}$. It means that these operators can be pre-processed or adaptively prepared in a table for further use in the course of Jacobian and residual assembly. These operator tables can also be re-used many times in the process of adjoint gradient assembly, reducing the time-consuming and complex evaluations of each property and its derivatives with respect to nonlinear unknowns.

Well treatment

The simulator utilizes a connection-based multi-segment well to simulate the flow in wells (Khait and Voskov, 2019). For BHP control, a fixed pressure constraint is added at the well block:

$$p - p^{target} = 0. \tag{B.6}$$

p^{target} is the target BHP at the well. The volumetric rate control is defined by the volumetric rate operator ζ_p^{vol} for given phase p:

$$\Gamma^l\zeta_p^{vol}(\boldsymbol{\omega})\Delta p - Q^{target} = 0, \tag{B.7}$$

where

$$\zeta_p^{vol} = \frac{\hat{s}_p(\boldsymbol{\omega})\beta_p(\boldsymbol{\omega})}{\hat{\rho}_t(\boldsymbol{\omega})}. \tag{B.8}$$

Q^{target} is the target volumetric flow rate, $\hat{s}_p$ and $\hat{\rho}_t$ are the saturation of phase p and total fluid density at production conditions, respectively. Eq. (B.6) and Eq. (B.7) are then coupled with energy boundary conditions:

$$\chi(\boldsymbol{\omega}) - T^{\text{target}} = 0, \tag{B.9}$$

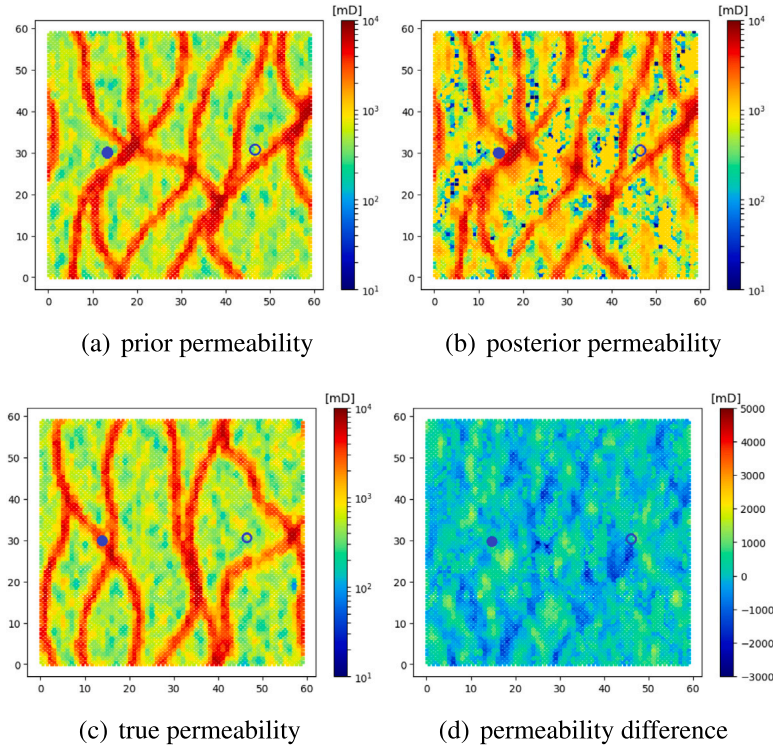

Fig. 15. The permeability distribution of the 4th layer of fluvial model. Figure (a) demonstrates the prior permeability of realization #66 before history matching; (b) is the posterior permeability after history matching; (c) shows the "true" permeability; and (d) demonstrates the permeability difference between posterior and prior based on the history matching constrained to ensemble prior mean. The blue dots and circles represent the injector and producer, respectively. (For interpretation of the references to color in this figure legend, the reader is referred to the web version of this article.)

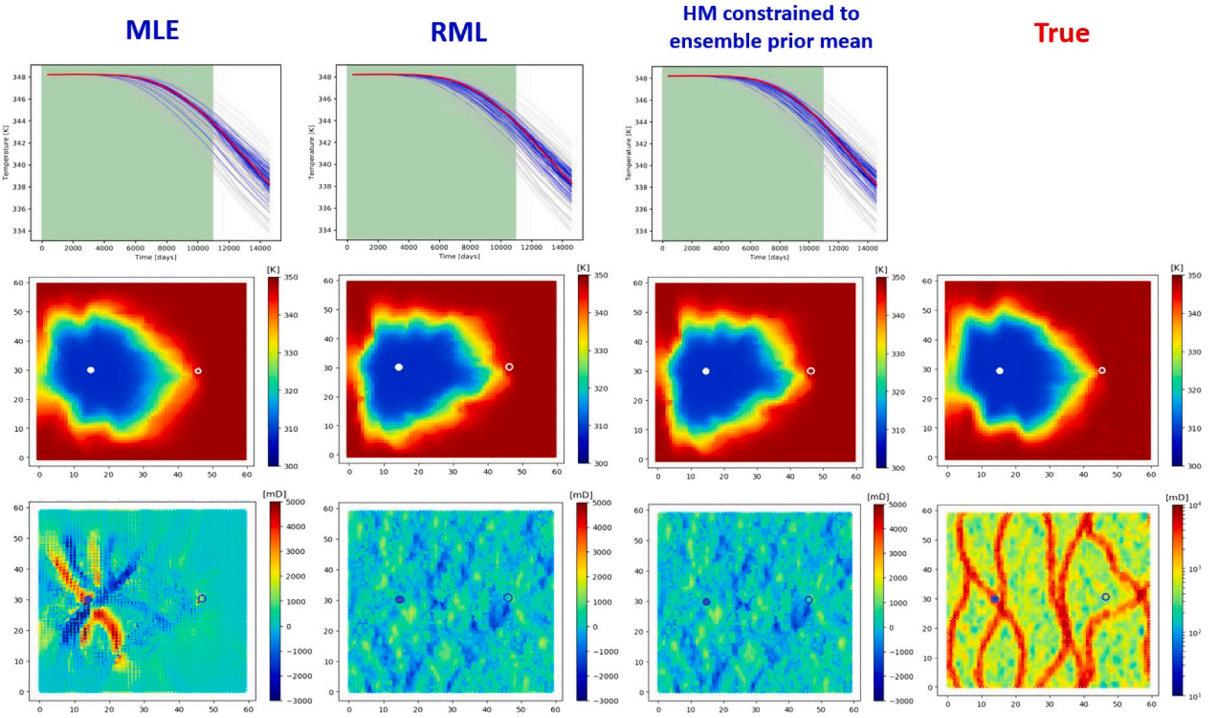

Fig. 16. The comparison of the history matching results is based on MLE (the first column), RML (the second column) and constrained to the ensemble prior mean (the third column). The true results are also included (the fourth column). From the top to the bottom rows, they represent the history matching results of producer well temperature, reservoir temperature distribution, and the permeability difference between the prior and posterior.

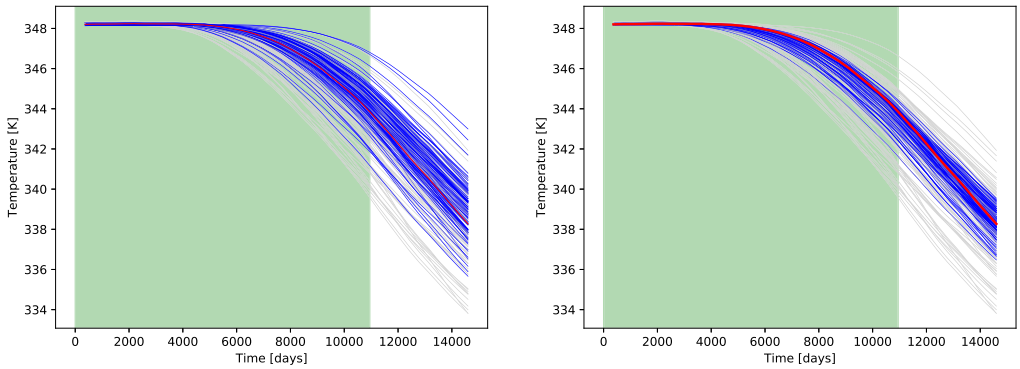

Fig. A.17. The history matching results of the well temperature based on RML under the original full space (left figure) and reduced-dimension ξ-space (right figure). The red curve is the observation data of well temperature. The gray and blue curves are the results before and after history matching, respectively. The green area shows the training period, while the white area is the forecasting period. (For interpretation of the references to color in this figure legend, the reader is referred to the web version of this article.)

where $\chi(\omega)$ is the temperature that is dependent on the thermodynamic state. T^{target} is the target temperature at the well.

Appendix C

The procedure of mapping the original model control variables $\boldsymbol{u}$ to $\boldsymbol{\xi}$ is described below. More details can be found in Vo and Durlofsky (2014), Sarma et al. (2007).

The covariance matrix can be calculated by using the following equation:

$$C_M = \frac{\boldsymbol{X}\boldsymbol{X}^T}{N_r - 1}, \tag{C.10}$$

where N_r is the total number of realizations, and $\boldsymbol{X}$ is given by:

$$\boldsymbol{X} = [\boldsymbol{u}_1 - \overline{\boldsymbol{u}}, \ldots, \boldsymbol{u}_{N_r} - \overline{\boldsymbol{u}}]. \tag{C.11}$$

$\boldsymbol{X}$ is a $N_u \times N_r$ matrix, where N_u is the number of the control variables in a single realization. The $\overline{\boldsymbol{u}}$ in Eq. (C.11) is the mean of the ensemble of the realization, and here we assume a Gaussian distribution for the model control variables $\boldsymbol{u}$. Instead of directly decomposing C_m, we perform Singular Value Decomposition (SVD) on the matrix $y = \boldsymbol{X}/\sqrt{N_r - 1}$ because of the decomposition efficiency. The factorized y using SVD is given:

$$y \approx \tilde{U}_{N_\xi} \tilde{\Sigma}_{N_\xi} \tilde{V}^T_{N_\xi}, \tag{C.12}$$

where $\tilde{\Sigma}$ is a diagonal matrix that contains the singular value of y, $\tilde{U}$ and $\tilde{V}$ are the unitary matrices that contain the left- and right-singular vectors of y respectively, the suffix N_ξ denotes the dimension size of the new parameter space (i.e. ξ-space) after the truncation to $\tilde{U}$, $\tilde{\Sigma}$, and $\tilde{V}$. The method of the prescribed portion of the variance (energy) contained in eigenvalues is used to determine N_ξ:

$$\frac{\sum_{k=1}^{N_\xi} \sigma_k^2}{\sum_{k=1}^{N_\Sigma} \sigma_k^2} \geq 90\%, \tag{C.13}$$

where σ_k is the square root of the eigenvalue (i.e. the element along the diagonal of $\tilde{\Sigma}$), N_Σ is the total number of the elements along the diagonal of $\tilde{\Sigma}$. Here we prescribe 90% as the energy portion value when determining the dimension of ξ-space. Once the dimension size N_ξ is determined, several important transformation matrices can be defined:

$$\boldsymbol{\Phi} = \tilde{U}_{N_\xi} \tilde{\Sigma}_{N_\xi}, \tag{C.14}$$

$$\hat{\boldsymbol{\Phi}}^{-1} = \tilde{\Sigma}^{-1}_{N_\xi} \tilde{U}^T_{N_\xi}, \tag{C.15}$$

$$\boldsymbol{\Psi} = \tilde{\Sigma}_{N_\xi} \tilde{U}^T_{N_\xi}. \tag{C.16}$$

The formulations of mapping between the original space and ξ-space are then written:

$$\boldsymbol{u} = \boldsymbol{\Phi}\boldsymbol{\xi} + \bar{\boldsymbol{u}}, \tag{C.17}$$

$$\boldsymbol{\xi} = \boldsymbol{\Phi}^{-1}(\boldsymbol{u} - \overline{\boldsymbol{u}}) \approx \hat{\boldsymbol{\Phi}}^{-1}(\boldsymbol{u} - \overline{\boldsymbol{u}}), \tag{C.18}$$

$$\nabla_\xi \mathcal{J} = \boldsymbol{\Phi}^T \cdot \nabla_u \mathcal{J} = \boldsymbol{\Psi} \cdot \nabla_u \mathcal{J}, \tag{C.19}$$

where $\boldsymbol{u}$ and $\boldsymbol{\xi}$ are the model control variables in the original space and the reduced-dimension ξ-space, respectively. $\nabla_\xi \mathcal{J}$ and $\nabla_u \mathcal{J}$ are the gradients of misfit term $\mathcal{J}$ with respect to the model control variable in the reduced-dimension ξ-space and the original space, respectively.

References

Adekitan, A.I., 2014. MONTE carlo simulation. http://dx.doi.org/10.13140/RG.2.2.15207.16806.

Bukshtynov, V., Volkov, O., Durlofsky, L.J., Aziz, K., 2015. Comprehensive framework for gradient-based optimization in closed-loop reservoir management. Comput. Geosci. 19 (4), 877–897. http://dx.doi.org/10.1007/s10596-015-9496-5.

Delft High Performance Computing Centre (DHPC), 2022. DelftBlue supercomputer (phase 1). https://www.tudelft.nl/dhpc/ark:/44463/DelftBluePhase1.

Donselaar, M.E., Groenenberg, R.M., Gilding, D.T., 2015. Reservoir geology and geothermal potential of the delft sandstone member in the west netherlands basin. In: Proceedings World Geothermal Congress.

Durlofsky, L., 2005. Upscaling and gridding of fine scale geological models for flow simulation. In: 8th International Forum on Reservoir Simulation Iles Borromees, Stresa, Italy, Vol. 2024. pp. 1–59. http://dx.doi.org/10.1016/j.advwatres.2016.07.019.

Fathi, Z., Ramirez, F.W., 1984. Optimal injection policies for enhanced oil recovery: Part 2-surfactant flooding. Soc. Petroleum Eng. J. 24 (03), 333–341. http://dx.doi.org/10.2118/12814-pa.

Faust, C.R., Mercer, J.W., 1979. Geothermal reservoir simulation: 1. Mathematical models for liquid- and vapor-dominated hydrothermal systems. Water Resour. Res. 15 (1), 23–30. http://dx.doi.org/10.1029/wr015i001p00023.

Gavalas, G., Shah, P., Seinfeld, J., 1976. Reservoir history matching by Bayesian estimation. Soc. Petroleum Eng. J. 16 (06), 337–350. http://dx.doi.org/10.2118/5740-pa.

Hoteit, I., Luo, X., Pham, D.-T., 2012. Particle Kalman filtering: A nonlinear Bayesian framework for ensemble Kalman filters. Mon. Weather Rev. 140 (2), 528–542. http://dx.doi.org/10.1175/2011mwr3640.1.

Jansen, J., 2011. Adjoint-based optimization of multi-phase flow through porous media - A review. Comput. & Fluids 46 (1), 40–51. http://dx.doi.org/10.1016/j.compfluid.2010.09.039.

Jansen, J.D., Fonseca, R.M., Kahrobaei, S., Siraj, M.M., Essen, G.M.V., den Hof, P.M.J.V., 2014. The egg model - A geological ensemble for reservoir simulation. Geosci. Data J. 1 (2), 192–195. http://dx.doi.org/10.1002/gdj3.21.

Khait, M., Voskov, D., 2018a. Adaptive parameterization for solving of thermal/compositional nonlinear flow and transport with buoyancy. SPE J. 23 (02), 522–534. http://dx.doi.org/10.2118/182685-pa.

Khait, M., Voskov, D., 2018b. Operator-based linearization for efficient modeling of geothermal processes. Geothermics 74, 7–18. http://dx.doi.org/10.1016/j.geothermics.2018.01.012.

Khait, M., Voskov, D., 2019. Integrated framework for modelling of thermal-compositional multiphase flow in porous media. In: Day 1 Wed, April 10, 2019. SPE, http://dx.doi.org/10.2118/193932-ms.

Khait, M., Voskov, D., Zaydullin, R., 2020. High performance framework for modelling of complex subsurface flow and transport applications. In: ECMOR 2020 - 17th European Conference on the Mathematics of Oil Recovery. http://dx.doi.org/10.3997/2214-4609.202035188.

Ma, X., Zabaras, N., 2011. Kernel principal component analysis for stochastic input model generation. J. Comput. Phys. 230 (19), 7311–7331. http://dx.doi.org/10.1016/j.jcp.2011.05.037.

Mehos, G.J., Ramirez, W., 1989. Use of optimal control theory to optimize carbon dioxide miscible-flooding enhanced oil recovery. J. Pet. Sci. Eng. 2 (4), 247–260. http://dx.doi.org/10.1016/0920-4105(89)90002-8.

Neuman, S.P., Guadagnini, A., Riva, M., Siena, M., 2013. Recent advances in statistical and scaling analysis of earth and environmental variables. In: Advances in Hydrogeology. Springer New York, pp. 1–25. http://dx.doi.org/10.1007/978-1-4614-6479-2_1.

Nikolaidis, E., Pandey, V., Mourelatos, Z., 2012. Managing the computational cost in a Monte Carlo simulation by considering the value of information. In: SAE Technical Paper Series. SAE International, http://dx.doi.org/10.4271/2012-01-0915.

Oliver, D.S., 1996. Multiple realizations of the permeability field from well test data. SPE J. 1 (02), 145–154. http://dx.doi.org/10.2118/27970-pa.

Oliver, D.S., Reynolds, A.C., Liu, N., 2008. Inverse Theory for Petroleum Reservoir Characterization and History Matching. Cambridge University Press, http://dx.doi.org/10.1017/cbo9780511535642.

O'sullivan, M.J., 1985. Geothermal reservoir simulation. Int. J. Energy Res. 9 (3), 319–332. http://dx.doi.org/10.1002/er.4440090309.

O'Sullivan, M., O'Sullivan, J., 2016. Reservoir modeling and simulation for geothermal resource characterization and evaluation. In: Geothermal Power Generation. Elsevier, pp. 165–199. http://dx.doi.org/10.1016/b978-0-08-100337-4.00007-3.

O'Sullivan, M.J., Pruess, K., Lippmann, M.J., 2001. State of the art of geothermal reservoir simulation. Geothermics 30 (4), 395–429. http://dx.doi.org/10.1016/s0375-6505(01)00005-0.

Oudshoorn, C., 2023. Data Assimilation for Geothermal Doublets Using Production Data and Electromagnetic Observations (Master's thesis). Delft University of Technology, URL http://resolver.tudelft.nl/uuid:ea00740d-d94e-4a10-a930-de4cf1740aa3.

Perkins, D., 2019. Reservoir Simulation for Play-based Development of Low Enthalpy Geothermal Resources (Master's thesis). Delft University of Technology, URL https://repository.tudelft.nl.

Ramirez, W.F., Fathi, Z., Cagnol, J.L., 1984. Optimal injection policies for enhanced oil recovery: Part 1 theory and computational strategies. Soc. Petroleum Eng. J. 24 (03), 328–332. http://dx.doi.org/10.2118/11285-pa.

Rath, V., Wolf, A., Bücker, H.M., 2006. Joint three-dimensional inversion of coupled groundwater flow and heat transfer based on automatic differentiation: sensitivity calculation, verification, and synthetic examples. Geophys. J. Int. 167 (1), 453–466. http://dx.doi.org/10.1111/j.1365-246x.2006.03074.x.

Rubinstein, R.Y., Kroese, D.P., 2007. Simulation and the Monte Carlo Method. Wiley, http://dx.doi.org/10.1002/9780470230381.

Rühaak, W., Guadagnini, A., Geiger, S., Bär, K., Gu, Y., Aretz, A., Homuth, S., Sass, I., 2015. Upscaling thermal conductivities of sedimentary formations for geothermal exploration. Geothermics 58, 49–61. http://dx.doi.org/10.1016/j.geothermics.2015.08.004.

Sanchez-Vila, X., Guadagnini, A., Carrera, J., 2006. Representative hydraulic conductivities in saturated groundwater flow. Rev. Geophys. 44 (3), http://dx.doi.org/10.1029/2005rg000169.

Sarma, P., Durlofsky, L.J., Aziz, K., 2007. Kernel principal component analysis for efficient, differentiable parameterization of multipoint geostatistics. Math. Geosci. 40 (1), 3–32. http://dx.doi.org/10.1007/s11004-007-9131-7.

Sarma, P., Durlofsky, L.J., Aziz, K., Chen, W.H., 2006. Efficient real-time reservoir management using adjoint-based optimal control and model updating. Comput. Geosci. 10 (1), 3–36. http://dx.doi.org/10.1007/s10596-005-9009-z.

Sen, P.N., Goode, P.A., 1992. Influence of temperature on electrical conductivity on shaly sands. Geophysics 57 (1), 89–96. http://dx.doi.org/10.1190/1.1443191.

Shetty, S., Voskov, D., Bruhn, D.F., 2018. Numerical strategy for uncertainty quantification in low enthalpy geothermal projects. In: Workshop on Geothermal Reservoir Engineering. URL https://pangea.stanford.edu/ERE/pdf/IGAstandard/SGW/2018/Shetty.pdf.

Stordal, A.S., vdal, G.N., 2017. A modified randomized maximum likelihood for improved Bayesian history matching. Comput. Geosci. 22 (1), 29–41. http://dx.doi.org/10.1007/s10596-017-9664-x.

Tian, X., Blinovs, A., Khait, M., Voskov, D., 2021. Discrete well affinity (DiWA) data-driven proxy model for production forecast. SPE J. 1–17. http://dx.doi.org/10.2118/205489-pa.

Tian, X., Voskov, D., 2022. Efficient application of stochastic discrete well affinity (DiWA) proxy model with adjoint gradients for production forecast. J. Pet. Sci. Eng. 210, 109911. http://dx.doi.org/10.1016/j.petrol.2021.109911.

Ucok, H., Ershaghi, I., Olhoeft, G.R., 1980. Electrical resistivity of geothermal brines. J. Pet. Technol. 32 (04), 717–727. http://dx.doi.org/10.2118/7878-pa.

Vo, H.X., Durlofsky, L.J., 2014. A new differentiable parameterization based on principal component analysis for the low-dimensional representation of complex geological models. Math. Geosci. 46 (7), 775–813. http://dx.doi.org/10.1007/s11004-014-9541-2.

Volkov, O., Voskov, D.V., 2015. Effect of time stepping strategy on adjoint-based production optimization. Comput. Geosci. 20 (3), 707–722. http://dx.doi.org/10.1007/s10596-015-9528-1.

Voskov, D., 2017. Operator-based linearization approach for modeling of multiphase multi-component flow in porous media. J. Comput. Phys. 337, 275–288.

Wang, Y., Voskov, D., Daniilidis, A., Khait, M., Saeid, S., Bruhn, D., 2023. Uncertainty quantification in a heterogeneous fluvial sandstone reservoir using GPU-based Monte Carlo simulation. Geothermics 114, http://dx.doi.org/10.1016/j.geothermics.2023.102773.

Wang, Y., Voskov, D., Khait, M., Bruhn, D., 2020. An efficient numerical simulator for geothermal simulation: A benchmark study. Appl. Energy 264, http://dx.doi.org/10.1016/j.apenergy.2020.114693.

Wei, L., Ramirez, W.F., Qi, Y.F., 1993. Optimal control of steamflooding. SPE Adv. Technol. Ser. 1 (02), 73–82. http://dx.doi.org/10.2118/21619-pa.

Wen, X.-H., Gómez-Hernández, J., 1996. Upscaling hydraulic conductivities in heterogeneous media: An overview. J. Hydrol. 183 (1–2), ix–xxxii. http://dx.doi.org/10.1016/s0022-1694(96)80030-8.

Werthmüller, D., Mulder, W., Slob, E., 2019. emg3d: A multigrid solver for 3D electromagnetic diffusion. J. Open Source Softw. 4 (39), 1463. http://dx.doi.org/10.21105/joss.01463.

Wu, H., Fu, P., Hawkins, A.J., Tang, H., Morris, J.P., 2021. Predicting thermal performance of an enhanced geothermal system from tracer tests in a data assimilation framework. Water Resour. Res. 57 (12), http://dx.doi.org/10.1029/2021wr030987.

Zhang, Y., Hoteit, I., 2020. Feature-oriented joint time-lapse seismic and electromagnetic history matching using ensemble methods. SPE J. 26 (03), 1341–1365. http://dx.doi.org/10.2118/203847-pa.

Zhang, Z., Jafarpour, B., Li, L., 2014. Inference of permeability heterogeneity from joint inversion of transient flow and temperature data. Water Resour. Res. 50 (6), 4710–4725. http://dx.doi.org/10.1002/2013wr013801.

Zhang, Y., Vossepoel, F.C., Hoteit, I., 2019. Efficient assimilation of crosswell electromagnetic data using an ensemble-based history-matching framework. SPE J. 25 (01), 119–138. http://dx.doi.org/10.2118/193808-pa.